PCFM 2023

6th International Conference on Physical Chemistry & Functional Materials

13-14 June 2023

Fırat University

ELAZIĞ / TÜRKİYE



BOOK OF FULL-TEXT ABSTRACTS

http://2023.pcfm-conference.com/

ISBN 978-605-80511-5-7

HONORARY CHAIR

Fahrettin GÖKTAŞ

Rector of Fırat University – Türkiye

HEAD OF CHAIR

Ömer KAYĞILI

Fırat University – Türkiye

Co-CHAIRS

Tankut ATEŞ

Malatya Turgut Özal University- Türkiye

Emine TANIŞ

Ahi Evran University - Türkiye

INTERNATIONAL ORGANIZING COMMITTEE

Octavio RONCERO *CSIC- Spain*

Cecilia COLETTI *University of Chieti - Italy*

Piotr ŻUCHOWSKI *Nicolaus C. University – Poland*

S.V. DOROZHKIN *Kudrinskaja sq. 1-155 - Russia*

LOCAL ORGANIZING COMMITTEE

Serhat KESER *Firat University – Türkiye*

Cihat AYDIN *Firat University - Türkiye*

Murat CANYILMAZ *Firat University - Türkiye*

Mehmet Mürşit TEMÜZ *Firat University – Türkiye*

İskender MUZ *Nevsehir Haci Bektas Veli University – Türkiye*

Özkan AÇIŞLI *Atatürk University - Türkiye*

SCIENTIFIC COMMITTEE

Abdulkadir YILDIZ *Kahramanmaraş Sütçü İmam University - Türkiye*

Ali TOZAR *Mustafa Kemal University - Türkiye*

Azeez A. BARZINJY *Soran University – Iraq*

Baha Vural KÖK *Firat University - Türkiye*

Beyhan TATAR *İstanbul University - Türkiye*

Cengiz TATAR *Firat University - Türkiye*

Fatih Ahmet ÇELİK *Bitlis Eren University – Türkiye*

Gürcan YILDIRIM *Abant İzzet Baysal University- Türkiye*

Hikmet KEMALOĞLU *Firat University - Türkiye*

Luis BAÑARES *Universidad Complutense - Spain*

Mediha KÖK *Firat University – Türkiye*

Mikail ET *Firat University - Türkiye*

Mosbah ZIDANI *University of Batna2 - Algeria*

Mustafa Burak TÜRKÖZ *Karabük University - Türkiye*

Nevin AYTEMİZ *Bandırma Onyedi Eylül University – Türkiye*

Niyazi BULUT *Firat University - Türkiye*

Ümit ERDEM *Kırıkkale University – Türkiye*

Yavuz ALTIN *Firat University - Türkiye*

SECRETARY

Ercan ERCAN *Bitlis Eren University - Türkiye*

Hanifi KEBIROGLU *Malatya Turgut Özal University - Türkiye*

Turan İNCE *Firat University – Türkiye*

İdil KARACA AÇARI *Malatya Turgut Özal University - Türkiye*

Rebaz OBAID KAREEM *University of Halabja - Iraq*

OPENING

Dear Participants,

On behalf of the organizing committee of the International Conference on **Physical Chemistry & Functional Materials (PCFM)** series, I would like to welcome you to our 6th conference in Elazığ.

The PCFM is an annual organization and was started firstly in Elazığ in 2018. The subsequent conferences were done in Cappadocia, Malatya, Elazığ (Online due to COVID-19), and Sivas. I would like to point out that this is a special honor for us that the 6th conference coincides with the 100th anniversary of the **Republic of Türkiye**.

The PCFM series covers all the essential sciences of Physics, Chemistry, Biology, and Engineering fields derived from the essential sciences.

We thank all the invited speakers, participants, and scientific and organizing committees for their invaluable contributions to the PCFM series.

Sincerely,

6th International Conference on Physical Chemistry & Functional Materials

PCFM-2023

BOOK OF ABSTRACTS

EDITOR

Ömer KAYĞILI, Ph.D.

Published, June 2023

This document is subject to copyright. All rights are reserved, whether the whole or part of the material is concerned. Nothing from this publication may be translated, reproduced, stored in a computerized system, or published in any form or any manner, including, but not limited to electronic, mechanical, reprographic, or photographic, without prior written permission from the publisher.

http://2023.pcfm-conference.com/ *omerkaygili@yahoo.com*

The individual contributions in this publication and any liabilities arising from them remain the responsibility of the authors.

The publisher is not responsible for possible damages, which could be a result of content derived from this publication.

ISBN: 978-605-80511-5-7

SPONSORS

FIRAT ÜNİVERSİTESİ 1975

TUĞBA ARISOY BEAUTY CENTER

ÜSTÜN HAFRİYAT-YIKIM

ELAZIĞ BOĞAZİÇİ HAVACILIK KOLEJİ

Materials Research Society of Serbia
24 conference
SERBIA MRS
YUCOMAT 2023
Herceg Novi, Montenegro : : September 4-8, 2023

PCFM 2023

6th International Conference on Physical Chemistry & Functional Materials

13-14 JUNE 2023

Firat University / ELAZIG

(IS: Invited Speaker, OP: Oral Presentation)

Time: UTC+3

Registration: 09:00 - 10:00

Opening Remarks: 10:00 - 10:15

Day-1 June 13, 2023

https://us06web.zoom.us/j/87664308696?pwd=c3NqRGpyUXdwQ0Z4d2tJT1dZTFE3UT09

Meeting ID: 876 6430 8696

Passcode: PCFM2023

Chair

Azeez Abdullah Barzinjy

10:15 -10:55	IS-2 **Dragan Uskokovic** Title: *Materials Research Fostering International Cooperation in Small and Developing Countries: The Example of Serbia*	Face to face
10:55-11:35	IS-1 **Nora de Leeuw** Title: *Discovering Bio-inspired Catalysts for CO_2 Conversion*	Face to face
11:35-12:15	IS-11 **Süleyman Köytepe** Title: *Design and Synthesis of Saccharide Based Polyurethanes for Sensor and Biomedical Applications*	Face to face
12:15-14:00	**Lunch**	

	Chair Nora de Leeuw	
14:00-14:40	IS-7 **Azeez Abdullah Barzinjy** Title: *Green Synthesis of Nanoparticles: From Preparation to Applications*	Face to face
14:40-15:10	IS-8 **Burhan Ateş** Title: *Nanoparticle-based Enzyme Carrier Matrixes for Enhance Catalytic Activity: A Promising Strategy*	Face to face
15:10-15:40	IS-10 **Savaş Kaya** Title: *Chemical Hardness and Fukui Potential Based Applications in Solid State Chemistry*	Face to face
15:40-16:00	**Coffee & Tea break**	
	Chair Dragan Uskokovic	
16:00-16:20	OP-11 **Serpil Yalçın Kuzu** Title: *Charged Vector Boson Research with Ensemble Learning Techniques*	Face to face
16:20-16:40	OP-42 **Ibrahim Isah Nasidi** Title: Polar Aprotic Solvent Acetonitrile Effect On Ascorbic Acid Using Different Quantum Models: A Theoretical Study	Face to face
16:40-17:00	OP-15 **Hazal Aktaş** Title: Evaluation of Mechanical Performances of Different Acrylic Resins used in 2K Varnish Systems	Face to face
17:00-17:20	OP-53 **Yasemin Merve Ayhan** Title: Theoretical Investigation of X-ray Radiation Absorption Mechanism of Yb-doped Sr-based Hydroxyapatites	Face to face

	Chair Mediha Kök	
17:20-17:40	IS-6 **Filiz Ercan** Title: *Structural Analysis of Nano Compounds by Using X-Ray Diffraction Method*	
17:40-18:00	IS-9 **İsmail Ercan** Title: *The Importance of ZnO in Scientific Research and The Effects Of The Magnetic Field*	
18:00-18:20	IS-5 **Ozkan Gokcekaya** Title: *The Role of Crystallographic Texture on Grain Boundary Characteristic Distribution for Defect Prevention in Metal Additive Manufacturing*	
18:20-18:40	OP-18 **İsmail Cem Kantarlı** Title: *Hydrochar Derived from Tomato Peel as Energy Feedstock and Adsorbent*	
18:40-19:00	OP-1 **Ahlam Abidi** Title: *The Classical Gauge Transformations and Their Effect on Entanglement*	
19:00-19:30	**Poster session**	
19:30-20:00	**Free time**	
20:00-21:30	**Gala Dinner**	

Day-2 June 14, 2023	https://us06web.zoom.us/j/83943821282?pwd=YOFHUGhtVkVVOUs2N1ZhbnVFNXhRdz09 Meeting ID: 839 4382 1282 Passcode: PCFM2023

	Chair Mediha Kök
09:00-09:30	IS-3 **Sergey V. Dorozhkin** Title: *Calcium Phosphate Bioceramics and Its Application in Medicine*
09:30-10:00	IS-4 **Mosbah Zidani** Title: *Exploitation of EBSD Data for the Analysis of the Crystallographic Texture of Industrial Metals*
10:00-10:10	OP-21 **Uğur Köroğlu** Title: Identification of Saliva Stains Through SERS Using Various Nanoparticles
10:10-10:20	OP-5 **Mokhtar Nebab** Title: Interfacial Stress Analysis of a Reinforced Concrete Beams Strengthened by Bonded Composite Plates Using a Deep-ANN Method
10:20-10:30	OP-4 **Sammia Shahid** Title: Designing of Photo-Catalysts Using Ternary Metal /G-C3N4/ZnO Nanocomposite for Effective Removal of Wastewater Pollutants
10:30-10:40	OP-2 **Ben Ammar Ben Khadda** Title: Effect of the Type of Concrete Curing by Renewable Energies on the Mechanical Performance in Southern Algeria
10:40-10:50	OP-3 **Navaad Zafar Ali** Title: Exploring the Dynamics of Molecular Rotors in Novel Framework Materials for Renewable Energy Technology

	Chair Serhat Keser	
10:50-11:00	OP-6 **Ali Çiriş** Title: Impact of $SnCl_2$ and $CdCl_2$ Heat Treatments on The Properties of SnS/CdS Stacks	
11:00-11:10	OP-7 **Merve Özcan** Title: Theoretical Computation of Structural and Electronic Structure Properties of Metal Halide Perovskite $CsSnBr_3$: A DFT Study	
11:10-11:20	OP-8 **Tuğrul Yumak** Title: From Waste Sawdust to Supercapacitors: Effect of Activation Type on The Electrochemical Performance of Activated Carbon	
11:20-11:30	OP-12 **Ceylan Alkaya** Title: Synthesis, Spectroscopic Analysis, DFT Studies and Molecular Insertion Applications of Isatin Hydrazone Derivative	
11:30-11:40	OP-13 **Adnan Aldemir** Title: Isotherm, Kinetic and Thermodynamic Studies of Toluidine Blue Adsorption onto Activated Carbon	
11:40-11:50	OP-14 **Gizem Durak Yüzüak** Title: Evaluation of Structural, Morphological and Electrical Properties of $Bi_4Sb_{38}Te_{58}$ Thin Film on Si(100)	
11:50-12:00	OP-16 **Tuğba Güngör Ertuğral** Title: Antibacterial Properties and Characterization of PLA Nanofibers Containing Lemon Cypress (Cupressus Macrocarpa Gold Crest) Essential Oil	
12:00-12:10	OP-24 **Margarita Goldberg** Title: The Oxidation of Benzyl Alcohol in the Presence of Mesoporous Molybdate-Contained Hydroxyapatite Powders	

	Chair Seçil Niksarlıoğlu
12:10-12:20	OP-25 **Işık İpek Avcı Yayla** Title: Ultrasound and Pressure Assisted Solid-State Polymerization of Carbazol
12:20-12:30	OP-26 **Ebru Yüce Babacan** Title: Composition of the Essential Oil of Endemic Gundelia Vitekii Species in Turkey
12:30-12:40	OP-27 **İlknur Baldan Işık** Title: Synthesis and Evaluation of Bimetallic $Pt_{62}Ni_{38}$ Electrocatalyst for Hydrogen Evolution Reaction
12:40-12:50	OP-28 **Tabti Affaf** Title: A Study of the Adsorption of a Polluting Organic Molecule in the Presence of Porous Materials
12:50-13:00	OP-29 **Erkan Karatas** Title: Development and Characterization of a Calcium Hydroxyapatite Based Injectable Formulation for Soft Tissue Augmentation
13:00-13:10	OP-66 **Özge Öztarakçı** Title: Investigation of Molecular Structures and Spectroscopic Properties of Iron Tetracarbonyl Nitrosyl Complex Isomers by Computational Methods
13:10-13:20	OP-23 **Boubekeur Razika** Title: Study of the Effect of Hydrophyl Polymers and Different Solvents on the Properties of Polysulfone Membranes
13:20-13:30	OP-22 **Alper Biçer** Title: Preparation of Waste Silica gel/Palmitic Acid (PA) Composite as a New Phase Change Material and Determination of its Thermal Properties
13:30-13:40	OP-35 **Nadezhda Donskaya** Title: The Oxidation of Benzyl Alcohol in the Presence of Mesoporous Tungsten-Contained Hydroxyapatite Powders

	Chair Cihat Aydın	
13:40-13:50	OP-36 **Seçil Sevim Ünlütürk** Title: Improvement of Nanomaterial Dispersibility by Hansen Solubility Parameters: The Ways of Scoring	zoom
13:50-14:00	OP-37 **İlayda Melek Çelik** Title: Powder Wettability Measurements of Fillers and Pigments Using the Washburn Capillary Rise Method	zoom
14:00-14:10	OP-38 **Necati Güdümcüoğlu** Title: Investigation of Organic Coating in Terms of Water Uptake Measurements by Electrochemical Impedance Spectroscopy	zoom
14:10-14:20	OP-32 **Erhan Karaca** Title: Review on Application of The XPS and XRD Techniques for Structural Characterization of Polypyrrole-Metal Oxide Based Anode Materials Used in Supercapacitors	zoom
14:20-14:30	OP-59 **Mehmet Hanifi Kebiroğlu** Title: Unraveling Ca-Phosphosilicate Molecule Fourier Transform Infrared (FTIR) Spectroscopy through Quantum Programming: A Comprehensive Investigation	zoom
14:30-14:40	OP-41 **Ayça Kıyak Yıldırım** Title: Electrodeposition of CdS Thin Films at Various Cathodic Potential Values	zoom
14:40-14:50	OP-39 **Rebaz Obaid Kareem** Title: Theoretical Investigation of chlorohydroquinone using Density Functional Theory and Hartree-Fock Method	zoom
14:50-15:00	OP-34 **Cihat Aydın** Title: Synthesis and Characterization of Al-SnO_2 Composite Films by Thermal Evaporation Method	zoom
15:00-15:10	OP-33 **Handan Aydın** Title: To be researched of optical and structural properties of Si doped TiO_2 thin films deposited on glass using Thermal Evaporation Method	zoom

	Chair Tankut Ateş	
15:10-15:20	OP-10 **Mehmet Mürşit Temüz** Title: Investigation of Metal-Ion Uptake Properties of Polystyrene	Face to face
15:20-15:30	OP-9 **Fatih İsen** Title: Williamson-Hall Analysis of Dysprosium-doped Hydroxyapatites	Face to face
15:30-15:40	OP-17 **Sevim Bilici** Title: Investigation of Optical Performance and Radiation Absorption Parameters of High Index Plastic Lens Material	Face to face
15:40-15:50	OP-19 **Muhammed Sait Kanca** Title: Coating of Glass Substrate with Sn Based Alloys Using Thermal Evaporation Systems	Face to face
15:50-16:00	OP-20 **Ercan Ercan** Title: Effect of Homogenization of CuAlTaNb Alloy in Liquid Nitrogen Medium on Thermal and Microstructural Properties	Face to face
16:00-16:10	OP-30 **Gonca Ateş** Title: Investigation of Optical Radiation and Absorption Parameters of Polarized Sunglasses	Face to face
16:10-16:20	OP-43 **Alev Taze** Title: Investigation of the Effects of Transition Metal W Doping on NiTiCu Alloy	Face to face
16:20-16:30	OP-45 **Ibrahim Isah Nasidi** Title: The Halogen Family Effect on the Bandgap of Ascorbic Acid: A Theoretical Study	Face to face
16:30-16:40	OP-46 **Ahmet Doğan** Title: X-Ray Diffraction Analysis of Zinc-based Quercetin-containing Hydroxyapatites	Face to face

	Chair Ercan Ercan	
16:40-16:50	OP-62 **Demet Coşkun** Title: Synthesis and Dielectric Properties of Three Armed Chalcone Derivatives	Face to face
16:50-17:00	OP-63 **Demet Coşkun** Title: Chalcone End Group Polymer Synthesis and Dielectric Properties	Face to face
17:00-17:10	OP-47 **Melikehatun Fırat** Title: Some Spectroscopic Properties of Silver-based Pyrocatechol-containing Hydroxyapatites	Face to face
17:10-17:20	OP-48 **Mehmet Çelik** Title: In vitro Anticancer Properties of Centaurea virgata Lam.	Face to face
17:20-17:30	OP-49 **Serhat Keser** Title: Antimicrobial, Antiradical Activities and Phytochemical Compounds of Wiedemannia orientalis Fisch. & Mey. Flowers	Face to face
17:30-17:40	OP-50 **Serhat Keser** Title: In vitro Cytotoxic Activities of Centaurea saligna (K.Koch) Wagenitz	Face to face
17:40-17:50	OP-31 **Emine Nur Acar** Title: An X-Ray Diffraction Study of Pr-Doped Hydroxyapatites Prepared by Ultrasonic-Assisted Wet Chemical Method	Face to face
17:50-18:00	OP-40 **Fatih Ahmet Çelik** Title: Molecular Dynamics Investigation of a Low-Alumina Calcium Alumina Silicate Glass-Ceramic System (%33CaO-%5Al2O3-%57SiO2-%5TiO2	Face to face
18:00-18:10	OP-60 **Meltem Coşkun** Title: Production of New Type Smart Composite Materials	Face to face
18:10-18:20	OP-61 **Mücahit Yılmaz** Title: Unveiling Ca-Phosphosilicate Molecule Nuclear Magnetic Resonance Spectroscopy through Quantum Programming: A Comprehensive Investigation	Face to face

18:20-18:30	OP-64 **Mehmet Yaşar** Title: The Relationship Between the Reaction Cross Section and The Geomagnetic Storm on 29 September 2016	Face to face
18:20-18:30	OP-65 **Mehmet Hanifi Kebiroğlu** Title: Investigation of Molecular Electrostatic Potentials for Serotonin, K-Serotonin and Ca-Serotonin	Face to face
18:30-18:40	OP-67 **Taner Daştan** Title: Experimental and Theoretical Investigations About Synthesis, Characterization, Biological Activity of Some New Coumarin Derivatives	Face to face
18:40-18:50	OP-68 **Taner Daştan** Title: Evaluation of Therapeutic Qualities of Propolis Samples from Sivas Province in Caenorhabditis elagans Cultures	Face to face
	Closing remarks	

TABLE OF CONTENTS OF FULL-TEXT PRESENTATIONS

ID	NAME & TITLE	PAGE
FTP-1	*Özge Öztarakçı* *Title: "Investigation of Molecular Structures and Spectroscopic Properties of Iron Tetracarbonyl Nitrosyl Complex Isomers by Computational Methods"*	001-008
FTP-2	*Ebru Yüce Babacan* *Title: "Composition of the Essential Oil of Endemic Gundelia Vitekii Species in Turkey"*	009-011
FTP-3	*Tuğba Güngör Ertuğral* *Title: "Preparation and characterization of PLA-based nanofibers containing antibacterial active lemon cypress (Cupressus macrocarpa gold crest) essential oil "*	012-016
FTP-4	*Ayça Kıyak Yıldırım* *Title: "Electrodeposition Of CdS Thin Films at Various Cathodic Potential Values"*	017-020
FTP-5	*Serpil Yalçın Kuzu* *Title: "Charged Vector Boson Research with Ensemble Learning Techniques"*	021-023
FTP-6	*Merve Özcan* *Title: "Theoretical Computation of Structural and Electronic Structure Properties of Metal Halide Perovskite CsSnBr3: A DFT Study "*	024-029
FTP-7	*Gizem Durak Yüzüak* *Title: "Evaluation of Structural, Morphological and Electrical Properties of Bi4Sb38Te58 Thin Film on Si(100) "*	030-036

FULL-TEXT PRESENTATIONS

FTP-1

Investigation of Molecular Structures and Spectroscopic Properties of Iron Tetracarbonyl Nitrosyl Complex Isomers by Computational Methods

Özge Öztarakçı, Duran Karakaş

Cumhuriyet University, Science Faculty, Chemistry Department, 50140, Sivas, Turkey

Abstract
eq-$[Fe(CO)_4(NO)]^+$ (**C_{2v}**), ax-$[Fe(CO)_4(NO)]^+$ (**C_{3v}**) and ax-$[Fe(CO)_4(NO)]^-$ (**C_s**) complex ions were designed for iron tetracarbonyl nitrosyl. Experimental C–O stretching frequencies of the complex with C_{2v} symmetry were used to determine the optimal computation level. The optimal level for the complexes was determined as BVP86/LANL2DZ/6-31G(d). Optimized structures of complex ions were found at the optimal computational level in the gas phase. From the bond angles, IR spectra and ^{13}C-NMR spectra, it was predicted that the iron atom in each of the complexes was a triangular bipyramidal ligand field.

Keywords: Metal carbonyls, Metal nitrosyls, Spectroscopic properties, Computational studies

1. Introduction

Metal carbonyls consisting of only CO and metal are called homoleptic, while metal carbonyls containing ligands other than carbonyl are called heteroleptic metal carbonyls. Iron carbonyls have important functions in many types of catalysis such as C-C bond formation, hydrogenation and amination [1,2].

A wide variety of model systems have been developed in recent years, especially regarding the importance of iron nitrosyl intermediates in biochemistry and medicine [3-6]. NO ligand can be linearly or angularly attached to the central metal atom. It is assumed that each type of bonding gives a different number of electrons to the metal. Iron tetracarbonyl nitrosyl complex ion with C_{2v} symmetry was synthesized by J. Bohnenberger and I. Krossing and some computational studies were carried out on the complex ion [7].

In this study, we considered that the NO ligand is linearly bonded to the central iron atom in the NO^+ form and angularly bonded in the NO^- form. We designed the schematic structures in Fig. 1. We aimed to investigate the molecular structures and spectroscopic properties of these complex ions using computational methods.

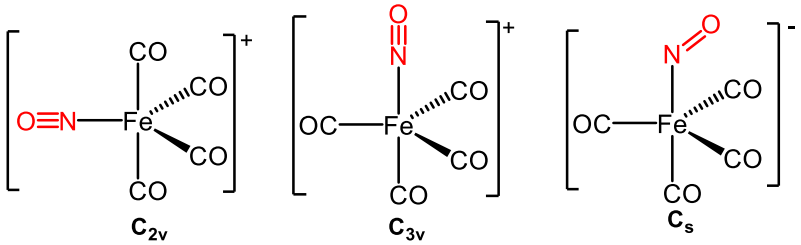


Fig. 1 Schematic structures of the studied complex ions.

2. Methods and Techniques

The structure of eq-$[Fe(CO)_4(NO)]^+$ (C_{2v}), ax-$[Fe(CO)_4(NO)]^+$ (C_{3v}) and ax-$[Fe(CO)_4(NO)]^-$ (C_s) complexes were drawn in Gauss View 6.0.16 program [8]. Benchmark analysis was performed according to the experimental C-O stretching frequencies of the complex with C_{2v} symmetry. The BVP86/LANL2DZ/6-31G(d) level was determined as the most optimal calculation level. Quantum chemical calculations were performed in the gas phase in the Gaussian 16 Revision C.01 program at the optimal calculation level [9]. The BVP86 method is a hybrid density functional theory (DFT) method. This method includes Becke88 exchange corrections [10] and Perdew86 correlation corrections [11]. LANL2DZ/6-31G(d) is a mixed basis set. The LANL2DZ basis set was used to model the iron atomic orbitals [12]. The 6-31G(d) polarized basis set was used to model the orbitals of C, N and O atoms in complex ions [13]. ^{13}C-NMR spectra and chemical shift values of the complexes at the BVP86/LANL2DZ/6-31G(d) level were calculated using the GIAO method.

3. Findings and Discussion

3.1 Benchmark analysis

The process of determining the optimal calculation level for an atomic or molecular system is called benchmark analysis. An experimentally measured property of the system is calculated at various levels in order to perform benchmark analysis. The level that gives the best agreement between the calculated and measured values is chosen as the optimal calculation level. For the eq-$[Fe(CO)_4(NO)]^+$ (C_{2v}) complex ion considered in this study, the C-O stretching frequencies were measured experimentally. Therefore, the CO stretching

frequencies of the conformer with C_{2v} symmetry were calculated at the levels of HF/LANL2DZ (1), HF/LANL2DZ/6-31G(d) (2), HF/DEF2TZVPP (3), B3LYP/LANL2DZ (4), B3LYP/LANL2DZ/6-31G (d) (5) B3LYP/DEF2TZVPP (6), BVP86/LANL2DZ (7), BVP86/LANL2DZ/6-31G(d) (8) and BVP86/DEF2TZVPP (9). The calculated harmonic C-O stretching frequencies are given in Table 1 together with the experimental frequencies.

Table 1 Calculated harmonic C-O stretching frequencies (cm^{-1}) for the eq-$[Fe(CO)_4(NO)]^+$ complex with C_{2v} symmetry, experimental frequencies and average of differences (AD)

Level	A_1	A_2	B_1	B_2	AD
1	2420	2415	2409	2408	266.2
2	2557	2553	2549	2547	405.7
3	2545	2540	2536	2535	393.2
4	2138	2100	2094	2079	43.0
5	2263	2228	2224	2210	85.5
6	2259	2219	2215	2199	77.2
7	2052	2000	1997	1980	138.5
8	2170	2122	2120	2105	16.5
9	2166	2113	2112	2094	24.5
Exp [7].	2183	2144	2137	2119	-

The average of the differences between the calculated and experimental frequencies can be taken as a benchmark. Therefore, the average of differences was calculated from eq. (1) and given in the last column of Table 1.

$$AD = \frac{|C - E|}{N} \quad (1)$$

Here, AD is the average of differences, C is the calculated value, E is the experimental value, and N is the number of values. The level with the lowest average of differences can be taken as the optimal calculation level. As can be seen from Table 1, lowest average of differences is level 8. This calculation level is BVP86/LANL2DZ/6-31G(d).

3.2 Ground state molecular structures

Molecular properties depend on molecular structures. Therefore, the determination of molecular structures has an important role in predicting molecular properties. Spectroscopic methods such as X-ray diffraction, IR, NMR are widely used to experimentally determine molecular structures. In order to determine the molecular structures computationally, molecular structure is optimized with optimal quantum chemical method and IR and NMR spectra of the molecule can be calculated. If a molecule is optimized by a suitable quantum chemical computational method, the optimized structures and the ORTEP diagrams obtained from the X-ray diffraction method almost overlap. The molecular structure parameters of the molecules can be found from the optimized structures obtained computationally.

The ground state molecular structures of the $[Fe(CO)_4(NO)]^{+/-}$ complex ions were optimized in the gas phase at the BVP86/LANL2DZ/6-31G(d) level and their optimized structures with atomic labeling are given in Fig. 2.

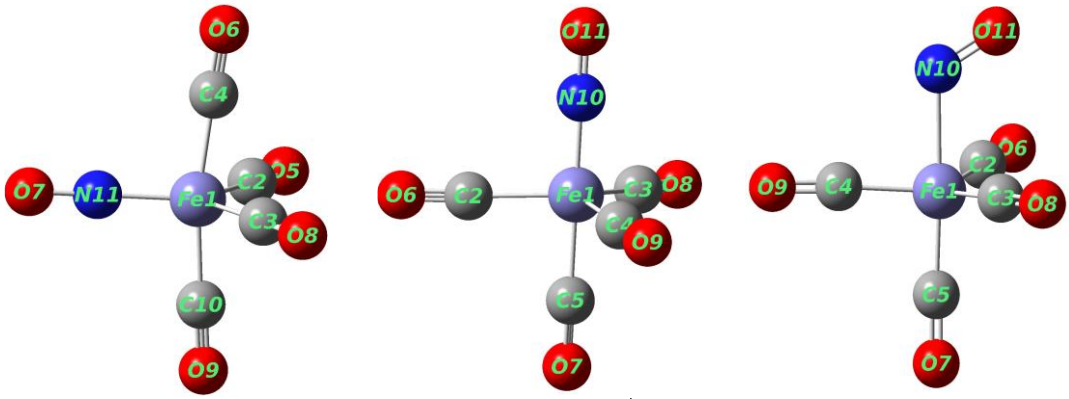


Fig. 2 Ground state molecular structures of $[Fe(CO)_4(NO)]^{+/-}$ complex ions obtained at the BVP86/LANL2DZ/6-31G(d) level

Some molecular structure parameters of the conformers with C_{2v}, C_{3v} and C_s symmetry of $[Fe(CO)_4(NO)]^{+/-}$ complex ions are given in Table 2. As seen in Table 2, equatorial Fe-C bonds are shorter than axial Fe-C bonds for all three complexes. This can be explained by the hybridization type of the iron atom in the complexes. In all of the complex ions, the central iron atom hybridized to dsp^3. Not all hybrid orbitals formed in this hybridization are identical. According to the Bent rule, dp hybrids form the axial Fe-C bonds and sp^2 hybrids form the equatorial Fe-C bonds [14]. Since the s-character of sp^2 hybrids is higher than the s-character of dp hybrids and the s orbitals are closer to the nucleus, equatorial Fe-C bonds are expected to be shorter than axial Fe-C bonds. Findings from the calculations confirm this prediction. In addition, the lengths of the experimental Fe-C bonds are given as 1.838 Å in the literature without making any axial-equatorial distinction [7]. Fe-N and N-O bonds in complex with Cs symmetry are longer than those of complexes with C_{2v} and C_{3v} symmetry, and Fe-C bonds are shorter. The longer Fe-N bond in the complex with C_s symmetry indicates that the NO^- ligand is weaker π-acceptor than the CO ligand. The strongest π-acceptor ligand in the spectrochemical series is CO. The CO ligand is isoelectronic with NO^+. Significant back bonding also occurs in NO^+ complexes. The longer N-O bond in the complex with C_s symmetry than that of the complexes with C_{2v} and C_{3v} symmetry is related to the degree of N-O bond. The degree of N-O bond is about three in the NO^+ ligand and about two in the NO^- ligand. The lower N-O bond degree in the NO^- ligand causes the N-O bond to be longer. As seen in Table 2, the C-O bonds in the complex with C_s symmetry are longer than those of the complexes with C_{2v} and C_{3v} symmetry. This result shows that the Fe-C bonds are strengthened in the C_s symmetrical complex, while the C-O bonds are weakened by back-bonding.

As seen in Table 2, the angles between the ligands in the equatorial positions are approximately 120°, the angles between the ligands in the axial positions are approximately 180°, and the angles between the ligands in the axial-equatorial positions are approximately 90°. These findings indicate that the central iron atom is a triangular bipyramidal ligand field.

Table 2 Some molecular structure parameters of the complexes

	C_{2v}	C_{3v}	C_s
Bond	Length (Å)	Length (Å)	Length (Å)
$Fe\text{-}C_{(eq)}$	1.838	1.837	1.767
$Fe\text{-}C_{(ax)}$	1.843	1.840	1.776
Fe-N	1.696	1.690	2.099
N-O	1.152	1.150	1.207
$C\text{-}O_{(eq)}$	1.150	1.150	1.181
$C\text{-}O_{(ax)}$	1.148	1.149	1.180
Angle	Degree (^{0})	Degree (^{0})	Degree (^{0})
$C_{(eq)}\text{-}Fe\text{-}C_{(eq)}$	113.3	119.3	121.5

$C_{(eq)}$-Fe-$C_{(ax)}$	87.3	85.2	91.9
$C_{(eq)}$-Fe-$N_{(eq)}$	123.3	-	-
$C_{(eq)}$-Fe-$N_{(ax)}$	-	94.8	85.5
$C_{(ax)}$-Fe-$C_{(ax)}$	170.1	-	-
$C_{(ax)}$-Fe-$N_{(ax)}$	-	180.0	177.7
Fe-N-O	180.0	179.9	120.5
Fe-$C_{(ax)}$-O	179.5	180.0	178.3
Fe-$C_{(eq)}$-O	178.4	178.3	178.8

3.3 IR Spectra in The Carbonyl Stretching Region and Symmetry Labeling of The Peaks

Since the C-O bond stretching frequencies in metal carbonyls are observed in a region that is quite different from the other bond stretching frequencies in the molecule (2200-1850 cm^{-1}), the molecular structure can be determined by considering only the C-O bond stretching modes. Therefore, this method is called the carbonyl factored force field method. There are studies on the applications of this method in the literature [15,16].

Applications of the carbonyl factored force field method propose C-O stretching peaks of symmetry species $2A_1+B_1+B_2$ for the complex with C_{2v}, $2A_1+E$ for the complex with C_{3v} and $3A'+A''$ for the complex with C_s symmetry. Since all vibrations of these symmetry species are IR active, four C-O stretching peaks should be observed for the complex with C_{2v} symmetry, three for the complex with C_{3v} (two C-O stretching peaks occur at the same frequency since the E symmetry species is binary degenerate) and four for the complex with C_s symmetry. IR spectra of the complexes in the C-O stretching region were calculated at the BVP86/LANL2DZ/6-31G(d) level and the symmetry labeling of the peaks are given in Fig. 3.

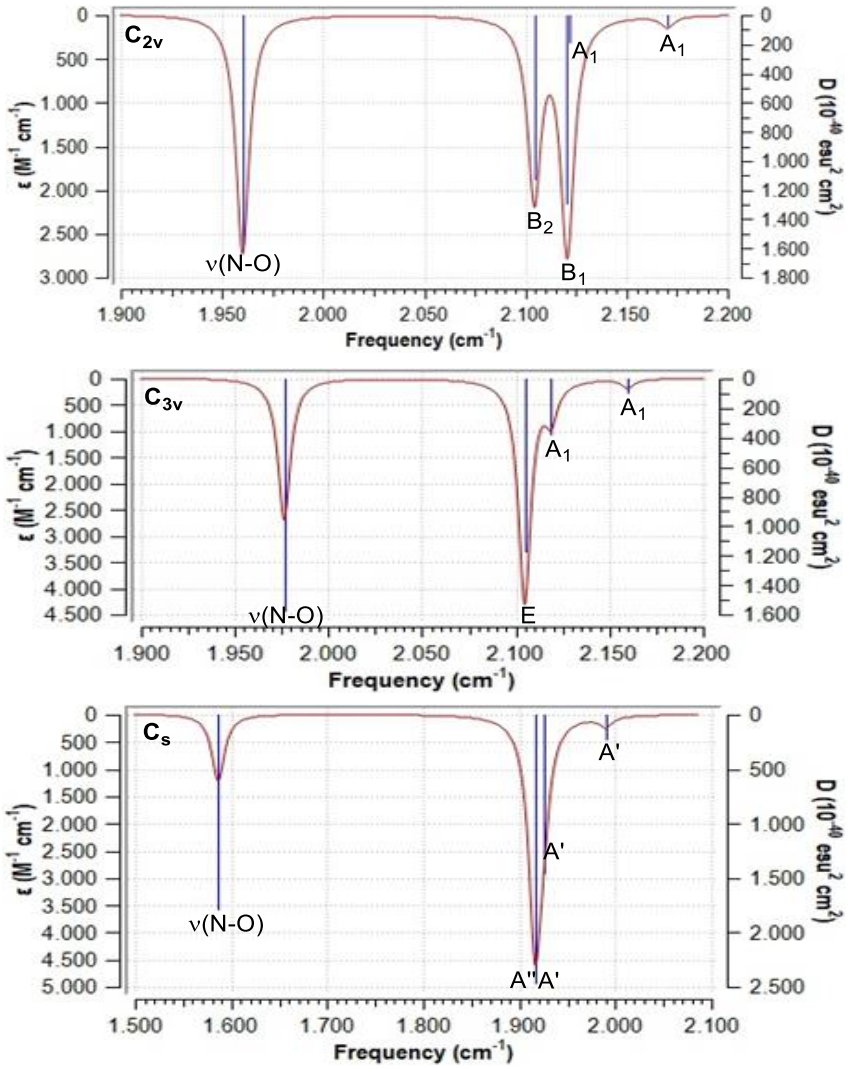


Fig. 3 IR spectra of the complexes with C_{2v}, C_{3v} and C_s symmetry calculated at the BVP86/LANL2DZ/6-31G(d) level and symmetry labeling of peaks.

Examining Fig. 3, the number of C-O peaks predicted by the carbonyl factored force fields method is observed for each of the complexes. The C-O stretching frequencies of the complex with Cs symmetry, which have A′ and A″ symmetries, are quite close to each other. Therefore, C-O stretching peaks with A′ and A″ symmetries appear as a single peak. The frequencies of the peaks are given in Table 3.

Table 3 Frequencies (cm^{-1}) of calculated C-O stretching peaks of complex ions

C_{2v}		C_{3v}		C_s	
symmetry	Frequencies*	symmetry	Frequencies	symmetry	Frequencies
A_1	2170.1 (2183)	A_1	2160.1	A′	1990.0
A_1	2122.0 (2144)	A_1	2119.0	A′	1925.0
B_1	2120.6 (2137)	E	2104.8	A′	1916.5
B_2	2104.5 (2119)	-	-	A″	1916.4

*Values in brackets are experimental values taken from Ref. [7].

As seen in Table 3, the C-O stretching frequencies of the complex with C_{2v} symmetry are greater than those of the complexes with C_{3v} and C_s symmetry. The high C–O stretching frequency can be explained by the fundamental equation (eq. 2) of IR spectroscopy [17].

$$\bar{\nu} = \frac{1}{2\pi c}\sqrt{\frac{k}{\mu}} \quad (2)$$

In the equation (2), k represents the force constant, μ the reduced mass of the bonded atoms, and $\bar{\nu}$ the vibrational frequency. The reduced mass for C-O has the same value in all complexes and the other parameters in the equation are constant. The bond stretching vibration frequency is then directly proportional to the square root of the bond force constant. In general, bond force constants are also directly proportional to bond dissociation energies. The higher the bond force constant, the higher the vibration frequency. According to this evaluation, the order of $k(C_s)<k(C_{3v})<k(C_{2v})$ can be made among the C-O bond stretching force constants of the complexes. A large C-O bond force constant indicates weak carbonyl back-bonding and a low Fe-C bond force constant. Angular binding and negative charge of NO^- ligand in this complex caused strong back-bonding, strengthening of Fe-C bonds and inhibition of CO emission by taking electrons from the central iron atom of the CO ligand to the π* molecular orbital. These findings obtained by vibration spectroscopy are also compatible with the bond lengths obtained from the optimized structures.

3.4 ^{13}C-NMR Spectra and Chemical Shift Values

Nuclear magnetic resonance (NMR) spectroscopy is a widely used technique for molecular structure determination. Equivalent and enantiotopic atoms in the molecule and their chemical shift values can be determined by NMR spectroscopy. Atoms that replace each other by rotation around an axis of symmetry are called equivalent atoms, and atoms that replace each other only by reflection are called enantiotopic atoms. Equivalent or enantiotopic atoms peak at the same chemical shift value in the NMR spectrum [17].

^{13}C-NMR spectra and chemical shift values of the complexes were calculated at the BVP86/LANL2DZ/6-31G(d) level using the Gauge-Independent Atomic Orbital (GIAO) method. TMS was used as reference. TMS was first optimized in the gas phase at the BVP86/6-31G(d). Then, the shielding of carbon atoms in TMS was calculated as 188.22 ppm with the GIAO method at the same level. Chemical shift values of carbon atoms in complex ions were calculated from eq (3).

$$\delta = \Sigma_{TMS} - \Sigma \quad (3)$$

Here, δ is the chemical shift value of carbon atoms according to TMS, Σ_{TMS} is the shielding of carbon atoms in TMS, and Σ is the shielding of carbon atoms in the complexes. The ^{13}C-NMR spectra of the complexes were calculated at the GIAO-BVP86/LANL2DZ/6-31G(d) level and the spectra are given in Fig. 4.

As seen in Fig. 4, there are two peaks with the same degeneracy in the ^{13}C-NMR spectrum of the complex with C_{2v} symmetry. Among these peaks, the low ppm value belongs to the 2C and 3C carbons in the equatorial position, and the high ppm value belongs to the 4C and 10C carbons in the axial position (Figure 2). This result shows that 2C-3C and 4C-10C are equivalent. As seen in Fig. 2, when the molecule with C_{2v} symmetry is rotated 180° around a C_2-axis passing through the Fe1-N11-O7 bond axis, 2C-3C and 4C-10C replace each other and are considered as equivalent atoms.

In ^{13}C-NMR spectrum of the complex with C_{3v} symmetry, there are two peaks with different degeneracy. According to this spectrum, 2C, 3C and 4C carbon atoms are equivalent. As can be seen from Fig. 2, these carbon atoms are in the equatorial position. When the molecule with C_{3v} symmetry is rotated 120° around a C_3 axis passing through the Fe1-N10-O11 bond axis, these carbon atoms replace each other and are equivalent atoms. In the C_{3v} complex, there is no other carbon atom to which 5C is equivalent.

The carbon atoms in the Cs symmetry complex are in three different chemical environments. In this complex, there is only the identity operation and the plane of symmetry. As can be seen from Fig. 2, the symmetry plane passes through the 2C-Fe1-3C bond bisector. When the molecule is reflected from this plane, 2C and 3C replace each other. Atoms that replace each other only by reflecting from a plane of symmetry are called enantiotopic atoms. Since enantiotopic atoms also give NMR peak at the same chemical shift value, 2C and 3C have the same chemical shift value. As seen in Fig. 4, NMR peak intensities or degeneracy are directly proportional to the equivalent atomic numbers. According to these evaluations, it can be said that the geometry of the central atom in the complexes is triangular bipyramidal.

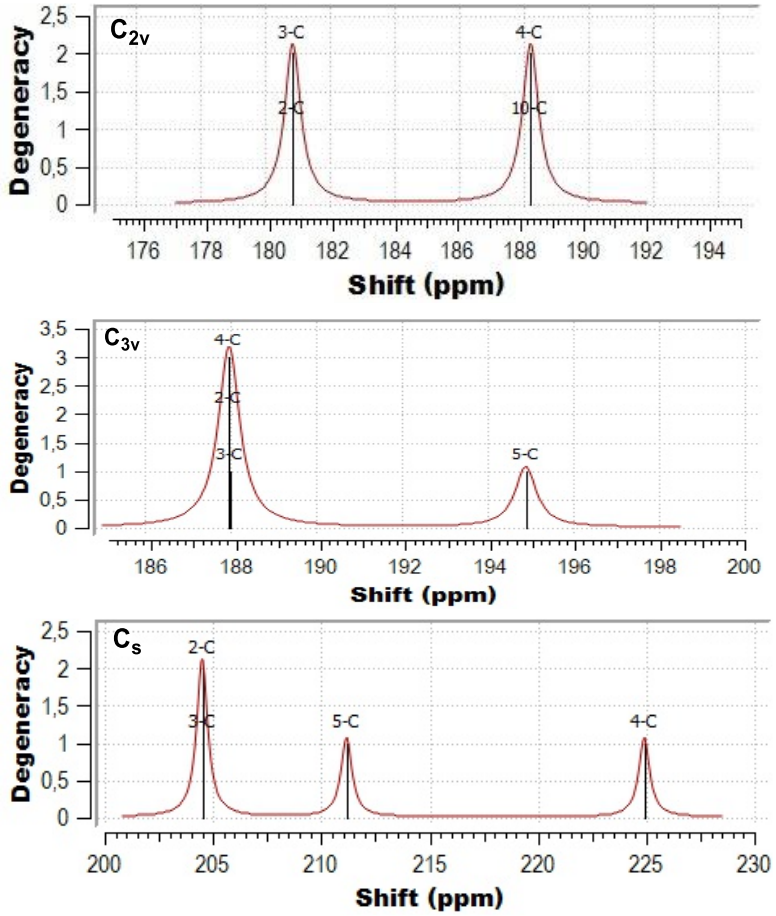


Fig. 4 ^{13}C-NMR spectra of the complexes with C_{2v}, C_{3v} and C_s symmetry calculated at the GIAO-BVP86/LANL2DZ/6-31G(d) level.

4. Conclusions

eq-$[Fe(CO)_4(NO)]^+$ (C_{2v}), ax-$[Fe(CO)_4(NO)]^+$ (C_{3v}) and ax-$[Fe(CO)_4(NO)]^-$ (C_s) complexes were designed. The optimal computational level was determined as BVP86/LANL2DZ/6-31G(d) using the experimental C-O stretching frequencies of the complex with C_{2v} point group. From the molecular structure parameters, IR and ^{13}C-NMR spectra, it was determined that the central iron atom in the complexes was in the triangular bipyramidal ligand field.

Acknowledgments

The authors are grateful for their support to the Sivas Cumhuriyet University, Scientific Research Unit (Project No: F-2022-663).

References

[1] Petricci, E., Santillo, N., Castagnolo, D., Cini, E., & Taddei, M. (2018). Iron-Catalyzed Reductive Amination of Aldehydes in Isopropyl Alcohol/Water Media as Hydrogen Sources. *Advanced Synthesis & Catalysis*, *360*(13), 2560-2565.

[2] Bromfield, K. M., Gradén, H., Ljungdahl, N., & Kann, N. (2009). Synthetic applications of cationic iron and cobalt carbonyl complexes. *Dalton Transactions*, (26), 5051-5061.

[3] Keilwerth, M., Hohenberger, J., Heinemann, F. W., Sutter, J., Scheurer, A., Fang, H., ... & Meyer, K. (2019). A Series of Iron Nitrosyl Complexes {Fe–NO} 6–9 and a Fleeting {Fe–NO} 10 Intermediate en Route to a Metalacyclic Iron Nitrosoalkane. *Journal of the American Chemical Society*, *141*(43), 17217-17235.

[4] Berto, T. C., Speelman, A. L., Zheng, S., & Lehnert, N. (2013). Mono-and dinuclear non-heme iron–nitrosyl complexes: Models for key intermediates in bacterial nitric oxide reductases. *Coordination Chemistry Reviews*, *257*(1), 244-259.

[5] In-Iam, A., Wolf, M., Wilfer, C., Schaniel, D., Woike, T., & Klüfers, P. (2019). {FeNO} 7-Type Halogenido Nitrosyl Ferrates: Syntheses, Bonding, and Photoinduced Linkage Isomerism. *Chemistry-A European Journal*, *25*(5), 1304-1325.

[6] Enemark, J. H., & Feltham, R. D. (1974). Principles of structure, bonding, and reactivity for metal nitrosyl complexes. *Coordination Chemistry Reviews*, *13*(4), 339-406.

[7] Bohnenberger, J., & Krossing, I. (2020). Stable Salts of Heteroleptic Iron Carbonyl/Nitrosyl Cations. *Angewandte Chemie International Edition*, *59*(14), 5581-5585.

[8] R.D. Dennington, T.A. Keith, J.M. Millam, GaussView 6.0. 16, Semichem. Inc., Shawnee Mission KS, 2016.

[9] M.J. Frisch, G.W. Trucks, H.B. Schlegel, G.E. Scuseria, M.A. Robb, J.R. Cheeseman, ... H. Nakatsuji, Gaussian09 Revision D. 01, Gaussian Inc., Wallingford CT, 2009,

[10] Becke, A. D. (1988). Density-functional exchange-energy approximation with correct asymptotic behavior. *Physical review A*, *38*(6), 3098.

[11] Perdew, J. P. (1986). Erratum: Density-functional approximation for the correlation energy of the inhomogeneous electron gas. *Physical review B*, *34*(10), 7406.

[12] Yang, Y., Weaver, M. N., & Merz Jr, K. M. (2009). Assessment of the "6-31+ G**+ LANL2DZ" mixed basis set coupled with density functional theory methods and the effective core potential: prediction of heats of formation and ionization potentials for first-row-transition-metal complexes. *The Journal of Physical Chemistry A*, *113*(36), 9843-9851.

[13] Csonka, G. I. (2002). Proper basis set for quantum mechanical studies of potential energy surfaces of carbohydrates. *Journal of Molecular Structure: THEOCHEM*, *584*(1-3), 1-4.

[14] Huheey, J. E. (1981). Bent's rule: energetics, electronegativity, and the structures of nonmetal fluorides. *Inorganic Chemistry*, *20*(11), 4033-4035.

[15] Karakaş, D., & Kaya, C. (2001). Force constant calculations for octahedral complexes of the type $M(CO)_5L$, based on the CO-factored force field. *Journal of organometallic chemistry*, *640*(1-2), 37-40.

[16] Kaya, C., & Karakas, D. (2007). Force constant calculations for $Hg[Co(CO)_4]_2$ from the CO-factored force field. *Indian journal of chemistry. Section A, Inorganic, bio-inorganic, physical, theoretical & analytical chemistry*, *46*(1), 33.

[17] Orchin, M., & Jaffé, H. H. (1971). *Symmetry, orbitals, and spectra (SOS)*. John Wiley & Sons.

FTP-2

Composition of the Essential Oil of Endemic *Gundelia Vitekii* Species in Turkey

Ebru Yüce Babacan, *[1] Azize Demirpolat [2]

[1]*Munzur University, Pertek Sakine Genç Vocational School, Tunceli, Türkiye*
[2]*Bingöl University, Vocational School of Food Agriculture and Livestock, Bingöl, Türkiye*

*ebruyuce@munzur.edu.tr

Abstract

In this study, essential oil composition of *Gundelia vitekii* of endemic to Turkey was studied for the first time. The essential oil composition of the examined plant was defined at a rate of 97.4% and is shown in Table 1. A total of 37 components were identified. Linoleic acid (49.3%), oleic acid (15.91%), palmitic acid (10.83%), 9,12-octadecadienoic acid (7.16%) and stearic acid (3.75%) are high components. This study provided new information about the essential oil compositions of the investigated species.

Introduction

In the historical process of the genus, *Gundelia tournefortii* was cited as the only species of the genus. However, numerous taxonomic studies in recent years reported that there have been 22 species of *Gundelia* definitioned over the years from the East Mediterranean region, Asia Minor, Transcaucasia, Iran and Afghanistan [1].

Gundelia species are widely consumed and used medicinally and traditionally. Local people use Kenger plant as egg meal with oli ve oil, watery food with rice, food with garlic yogurt, salad, pickle, gum, coffee, snack and animal feed [2].

In recent years, there have been many chemical studies of the *Gundelia tournefortii* [3]. In this study, essential oil analysis of endemic *Gundelia vitekii* was were determined for the first time.

Materials and Methods

Collection of plant material

Gundelia vitekii, which constitutes the study material, was collected in Elazig province (B7 Elazig: Sivrice, Hazar Baba mountain road, 15. km, roadside, 01.06.2021, E. Yüce 4030) in June 2021 with flowers. The aerial parts of the plant were used for analysis. After its diagnosis, it is prepared in accordance with herbarium techniques and kept in Fırat University

Preparing GC-MS Sample

1 g plant specimen is scaled, then 5 ml hexane/isopropanol (3:2) is added on. It is centrifuged for 10 minutes in 5000 rpm. The upper part is taken and put it into test tubes with filtered. It is vortexed with adding 2.5 ml from 2% methanolic sulfuric acid on it. This mixture is waited in 50 ^{0}C drying-oven for 15 hours. After 15 hours, the tubes are taken out and cooled until room temperature and vortexed with adding 2.5 ml 5% NaCl. Fatty acid methyl esters in the tubesare extracted with 2.5 ml hexane. The hexane phase is taken with a pasteur pipette and treated with 2.5 ml of 2% Na_2CO_3 and allowed for 1 hour to separate the phases. The upper phase is added to test tubes. The solvent of the mixture containing methyl esters is the nevaporated under nitrogen at 45 ^{o}C and the fatty acids at the bottom of the test tubesare dissolved in 1 ml of hexane and taken up in GC vials by mouth-capand analyzed on a GC-MS device.

GC-MS Device Method

For essential oil extraction, Agilent brand 7890A model GC, 5975C model MS and FID detector were used simultaneously. Colon BPX90 (100m x 0,25 mm x 0,25 µm) Colon Flow Rate (transporter gas helium). Chromatographic conditions: Starting at 120 °C, it reaches 254 °C at 5 °C/min and wait shere for 16 minutes. Total analysis time is 43 min. Injection volume was selected 1 µl and splitless mode was selected too. MS results were compared with the Wiley and Nist libraries in the device memory.

Results and Discussion

Essential oil components obtained from the aerial parts of the endemic *G. vitekii* plant by water distillation were determined. These components were determined by GC/MS, GC (Gas Chromatography) and MS (Mass Spectrometry). The essential oil yield of this species is 100 gr. It was found to be 0.5 ml over the sample. The essential oil composition of the examined plant was defined at a rate of 97.4% and is shown in Table 1. A total of 37 components were identified. Linoleic acid (49.3%), oleic acid (15.91%), palmitic acid (10.83%), 9,12-octadecadienoic acid (7.16%) and stearic acid (3.75%) are high components.

In the analysis of the volatile oil from aerial parts of *G. tournefortii* [4]; α-terpinyl acetate (36.21 %), methyl eugenol (12.57 %), eugenol (6.7 %), β-caryophellene (5.94 %) and zingiberene (5.84 %) were found as the major oil components. Present analysis results were not similar with this study (Halabi); findings, because of the absent of the major components (except β-caryophyllene) in present samples.

In a 2016 study, the essential oil from the aerial parts of *Gundelia tournefortii* was extracted using steam distillation method [5]. A total of 18 compounds, representing 88.4% total fat content was determined. A terpinyl acetate (15.2%), eugenol (9.5%), pcyme (9.5%), β-caryophyllene (7.1%) and estragole (6.1%), were the main components.

Gundelia tournefortii L. is an important food source and a well-known medicinal plant in Iran. A total of 41 compounds representing 96.2% of the volatile oil were identified. The main constituents were thymol (11.2%), γ-terpinene (9.8%), germacrene D (6.6%) and *p*-cymene (6.3%) [6].

Conclusions

In this study, essential oil composition of *Gundelia vitekii* of endemic to Turkey was studied for the first time. This study provided new information about the essential oil compositions of the investigated species.

Gundelia tournefortii and other species of the genus have been recognized as a nutritious food in the world and in Turkey, and the results highlight the importance of these plants to local people and support efforts towards industrial use, conservation, renewable resources, and food nutrition and additives.

References

1. IPNI. International Plant Names Index. Published on the Internet http://www.ipni.org, The Royal Botanic Gardens, Kew, Harvard University Herbaria & Libraries and Australian National Herbarium. [Retrieved 24 May 2023].
2. U. Çakılcıoglu, An ethnobotanical field study; traditional foods production and medicinal utilization of Gundelia L. species in Tunceli (Turkey). Indian Journal of Traditional Knowledge, 2020, **19**, 714-718.
3. J. Asghari, T. Bagheri, A. Shakeri, Arznei-Gewurzpfla, A systematic review of medicinal and molecular perspective. Pakistan Journal of Biological Sciences, South African Journal of Botany, 2015, **20**, 122–126. E. Qnais, Y. Bseiso, M. Wedyan, M. Al-Omari, H. Alkhateeb, Chemical composition and antinociceptive effects of essential oil from aerial parts of Gundelia tournefortii L. Asteraceae (Compositae) in rats. Trop. J. Pharm. Res. 2016, **15**, 2183–2190. S. Han, A. Ahmeda, A.R. Jalalvand, W. Lu, M.M. Zangeneh, Application of silver nanoparticles containing Gundelia tournefortii L. leaf aqueous extract in the treatment of microbial diseases and cutaneous wound healing. Appl Organometal Chem. 2020. S. Gezici, N. Sekeroglu, Comparative biological analyses on kenger and kenger coffee as novel functional food products. J Food Sci Technol, 2022, **59**, 2328–2338
4. S. Halabi, A.A. Battah, T. Aburjai, M. Hudaib, Phytochemical and antiplatelet investigation of Gundelia tournefortii. Pharm. Biol., 2005, **43**, 496-500.
5. E. Qnais, Y. Bseiso, M. Wedyan, M. Al-Omari, H. Alkhateeb, Chemical composition and antinociceptive effects of essential oil from aerial parts of Gundelia tournefortii L. Asteraceae (Compositae) in rats. Trop. J. Pharm. Res. 2016, **15**, 2183–2190.
6. D. Dastan, M. Yousefzadi. Volatile oil constituent and biological activity of Gundelia tournefortii L. from Iran. Journal of Reports in pharmaceutical sciences, 2016, **5**(1), 18-24.

Table 1. Constituents of the essential oils from *Gundelia vitekii*

Number	**Compounds**	**RRI**	***Gundelia vitekii***
			% concentration
1	Methyl-9-(tert-butydiml) ethylsiloxy)-6-ethyl-2,4-nonadienoate	2035	0.22
2	Decane	2197	0.08
3	Pentadecane	2241	0.27
4	Decane, 5-methyl-	2258	0.03
5	Decane, 4-methyl-	2262	0.04
6	Dodecane	2453	0.05
7	n-tetradecane	2521	0.36
8	Undecane	2595	0.26
9	Docosane	2752	0.10
10	n-tetracosane	2770	0.22
11	n-eicosane	2781	0.21
12	Tricosane	2860	0.02
13	Dodecane, 2-methyl	2983	0.04
14	Heneicosane	3021	0.08
15	Octadecane, 1-iodo-	3298	0.04
16	Hentriacontane	3325	0.11
17	Benzaldehyde, 4-proply-	3362	0.37
18	Myristic acid	3641	0.20
19	Isopropyl myristinate	3696	0.09
20	2(3H)-Furanone, 5-butyldihydro-	3785	0.09
21	Nonanedioic acid, dimethyl ester	3961	0.05
22	Lauryl alcohol	4029	0.10
23	3-heptadecanol	4101	0.37
24	Palmitic acid	4195	**10.83**
25	Isopropyl palmitate	4259	1.32
26	2,4-di-tert-butylphenol	4439	2.66
27	Stearic acid	4932	**3.75**
28	Oleic acid	5027	**15.91**
29	Propyl 9-octadecenoate	5094	1.81
30	Propyl 11-octadecenoate	5127	0.15
31	Linoleic acid	5241	**49.30**
32	9,12-octadecadienoic acid	5287	**7.16**
33	□□linoleic acid	5508	0.22
34	Benzenepropanoic acid	5574	0.49
35	Eicosatrienoic acid	5851	0.31
36	Docosanoic acid, methyl ester	7194	0.04
37	Decosapentaenoic acid	7199	0.05
	Total		**97.4**

FTP-3

Preparation and characterization of PLA-based nanofibers containing antibacterial active lemon cypress (Cupressus macrocarpa gold crest) essential oil

Tuğba Güngör Ertuğral

Faculty of Çanakkale Applied Sciences, Department of Food Technology, Çanakkale Onsekiz Mart University, Çanakkale, Türkiye

Nanofibres produced by electrospin technique and containing antimicrobial compounds for foods as packaging material. Biodegradable Polylactic acid (PLA), which can replace traditional plastics, is an economical and environmentally friendly polymer. In this study, essential oil of lemon cypress (*Cupressus macrocarpa gold crest*) (CMEO) was used. Antibacterial properties of CMEO against *Staphylococcus aureus* and *Escherichia Coli* were investigated and PLA-based PLA/CMEO nanofibres were produced that is containing 5%, 10%, 20% essential oils and nonofibres were characterized by Fourier Transform Infrared (FTIR), Scanning Electron Microscopy (SEM) and Thermogravimetric Analysis (TGA). Microbial analysis results showed that CMEO was effective against *Staphylococcus aureus* and *Escherichia Coli*. SEM results of nanofibres shows a fiber diameter of approximately 77.73 nm in PLA/CMEO nanofibre which is containing 20% CMEO. According to TGA analysis results, nanofibres have highest degradation rate at approximately 325ºC.

Keywords: PLA, Essential Oil, Food Packaging Material, Electrospin.

Introduction

The biological effect of essential oils obtained from plants is a known fact since ancient times [1]. Such that essential oils of Egyptian *Cupressus macrocarpa*, which is a candidate to be used as paharmatic and antimicrobial activity in food industry, are highly bioavailable and have strong sensory properties [2].

Polylactic acid (PLA) was discovered at low molecular weight in 1932 by DuPont scientist Wallace Caruthers [3]. The polymerization of PLA requires the monomer lactic acid (LA) with the molecular formula is $C_3H_6O_3$ [4]. PLA polymer is aliphatic and produced from natural products such as corn, starch and sugar cane [5]. Electrospin method is an economical method for fibers with nano diameter [6]. Electrospinning can be briefly explained as production of fibers in submicron fineness by applying electrostatic forces to a polymer solution or melt [7,8].

In this study, antibacterial properties of CMEO essential oil were examined and containing 5%, 10% and 20% CMEO; PLA/CMEO1, PLA/CMEO2 and PLA/CMEO3 nanofibres were produced by electrospin method and characterized by Fourier Transform Infrared (FTIR), Scanning Electron Microscope (SEM) and Thermogravimetric Analysis (TGA).

Material and Method

Materials

Dimethyl formamide (DMF) and Polylactic acid (PLA) were purchased from Sigma-Aldrich. 100% pure *Cupressus macrocarpa gold crest essential oil* was commercially purchased from BAÇEM Balıkesir Metropolitan Municipality Rural Services/ TÜRKİYE.

Cupressus macrocarpa gold essential oil (CMEO) antibacterial test

The standard disk diffusion method of CLSI was used to test antibacterial activity of plant essential oils (CLSI, 2006) [9]. Bacterial suspension at 100 µm (0.5 McFarland turbidity) was spread on Luria Bertani Agar (LBA) plate. Test material was placed on LBA and incubated at 24 hours and 37°C and measured to diameters of inhibition [10,11].

Preparation of PLA/CMEO nanofibres

While preparing nanofibres, 0.4 g of PLA was dissolved in 5 ml of DMF (v/v) CMEO was added to dissolved polymer and injected into a 5 ml syringe. With NE 100 electrospining system (Inovenso LLC. Istanbul, Turkey) at 17 kV, 25 ºC and solution flow rate is 0.62 mL/h (New Era Pump Systems, Farmingdale, NY) and distance at 17.0 cm adjusted and applied [12].

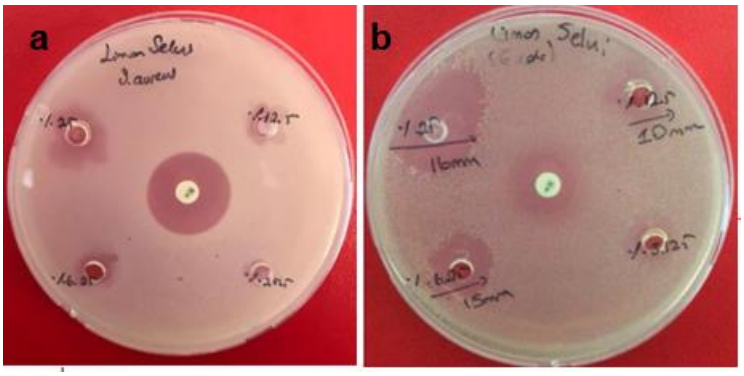
Characterization of PLA/CMEO nanofibres

FTIR analysis of PLA and pure PLA nanofibres was performed with a spectrum 100 FT-IR spectrometer and transmission mode at resolution of 4 cm^{-1} and nanofibres were scanned at wavelengths between 4000 cm^{-1} and 650 cm^{-1} [13]. TGA analysis of nanofibres shows that

thermal degradation of PLA and pure PLA nanofibres was determined with TGA 8000 Perkin Elmer, USA between 0-700 ºC at heating rate of 10 °C min^{-1} under a nitrogen atmosphere [14]. SEM images were analyzed with a high resolution Carl Zeiss 300VP capable of sensing 150 Pa pressure using real lenses powered by Gemini SEM Technology and featuring Nano VP reducing beam broadening [14,15].

Result And Discussion

In the CMEO antibacterial effect test, inhibition zones of 10 mm against *S. aureus* and 16 mm against *E. Coli* were formed at petri dishes in trials with certain percentages of CMEO. Considering diameter sizes, it can be said that CMEO is effective against *S.aureus* and *E.Coli* at certain rates (Picture 1) [16].



Picture 1. Activity of *Cupressus macrocarpa gold essential oil* against *S.aureus*(a) and *E.Coli* (b)

According to FTIR analysis, relative strength of the peak at 1762 cm^{-1}, which belongs to carbonyl group in PLA, also decreased with additional of essential oils. For PLA/CMEO blends, these peaks were net in pure PLA. The result corresponded to a decrease in tensile property with inclusion of CMEO (Fig.1). TGA curves of PLA/CMEO3 nanofibre shows that maximum degradation rate of nanofibre is about 325°C (Fig.2) [17].

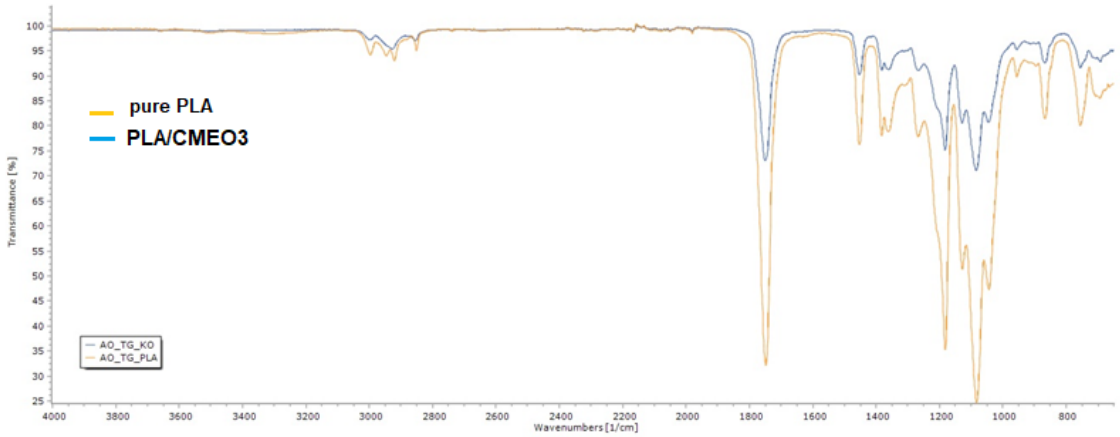


Figure 1. FTIR spectrum of pure PLA and PLA/CMEO3 nanofibres

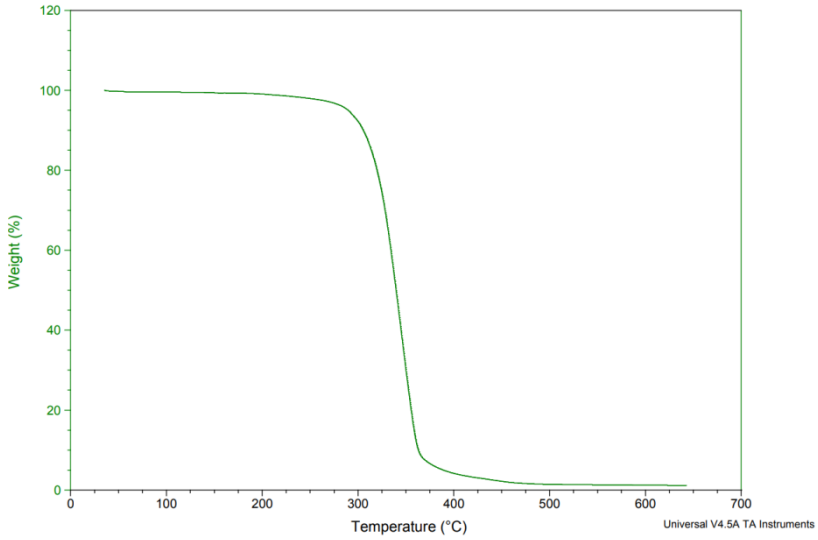


Figure 2. TGA curve of PLA/CMEO3 nanofibre

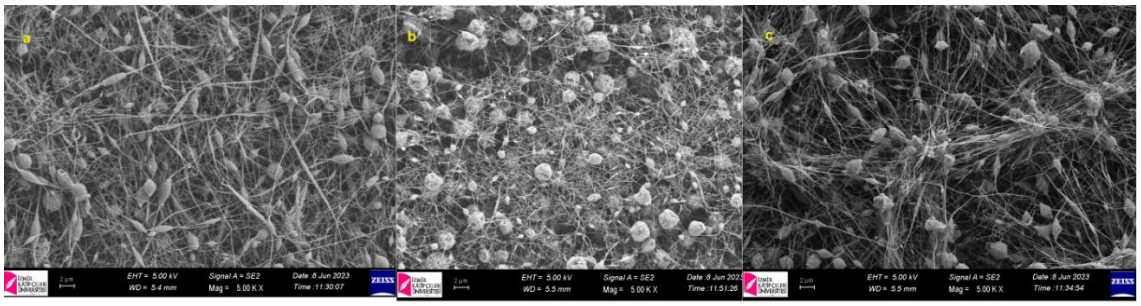


Figure 3. SEM images of PLA/CMEO1(a), PLA/CMEO2(b) and PLA/CMEO3(c)

According to results of SEM analysis, CMEOs were prominent on nanofiber (Fig.3) and film density decreased with increase of the oil percentage [18]. Diameter of PLA/CMEO3 nanofiber was measured as 77.73 nm (Fig. 4).

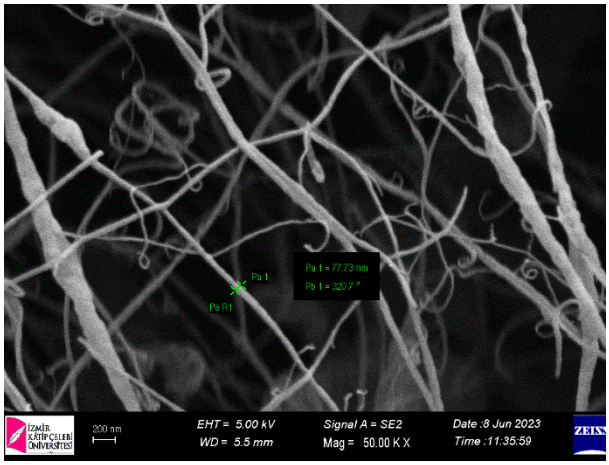


Figure 4. SEM image of PLA/CMEO3 nanofibre

Conclusion

In this study, it was seen that PLA formed composite with CMEO and nanofibre was formed successfully. *Cupressus macrocarpa gold essential oil* is effective against *S.aureus* and *E.Coli* bacteria, and nanofibres produced by dispersing essential oil in PLA may also gain antibacterial properties [16]. TGA result of PLA/CMEO3 composite nanofibre which has highest essential oil content nanofibres was examined and maximum degradation was observed at approximately 325ºC [17]. Use of PLA/CMEO nanofibres can benefit for food, pharmaceutical and cosmetic industries.

Acknowledgment

This study was funded by Çanakkale Onsekiz Mart University Scientific Research (BAP) project code FHD-2022-3969.

References

1. Hay, R. K., & Waterman, P. G. (1993). *Volatile oil crops: their biology, biochemistry and production*. Longman Scientific and Technical.

2. El-Ghorab, A. H., El-Massry, K. F., & Shaaban, H. A. (2007). Effect of drying on the chemical composition of the Egyptian Cupressus macrocarpa (Hartw. ex Gordon) essential oils and their biological characteristics. Journal of essential oil bearing plants, 10(5), 399-411.

3. Carothers, W. H. (1929). Studies on polymerization and ring formation. I. An introduction to the general theory of condensation polymers. *Journal of the American Chemical Society*, *51*(8), 2548-2559.

4. Datta, R., & Henry, M. (2006). Lactic acid: recent advances in products, processes and technologies—a review. *Journal of Chemical Technology & Biotechnology: International Research in Process, Environmental & Clean Technology*, *81*(7), 1119-1129.

5. Yoruç, A. B. H., & Uğraşkan, V. (2017). Yeşil Polimerler ve Uygulamaları. *Afyon Kocatepe Üniversitesi Fen ve Mühendislik Bilimleri Dergisi*, *17*(1), 318-337.

6. Chronakis, I. S. (2005). Novel nanocomposites and nanoceramics based on polymer nanofibers using electrospinning process—A review. *Journal of materials processing technology*, *167*(2-3), 283-293.

7 Chong, E. J., Phan, T. T., Lim, I. J., Zhang, Y. Z., Bay, B. H., Ramakrishna, S., & Lim, C. T. (2007). Evaluation of electrospun PCL/gelatin nanofibrous scaffold for wound healing and layered dermal reconstitution. *Acta biomaterialia*, *3*(3), 321-330.

8. Li, D., Wang, Y., & Xia, Y. (2004). Electrospinning nanofibers as uniaxially aligned arrays and layer-by-layer stacked films. *Advanced materials*, *16*(4), 361-366.

9. Wayne, P. A. (2010). Clinical and Laboratory Standards Institute: Performance standards for antimicrobial susceptibility testing: 20th informational supplement. *CLSI document M100-S20*.

10. Hufford, C. D., Funderburk, M. J., Morgan, J. M., & Robertson, L. W. (1975). Two antimicrobial alkaloids from heartwood of Liriodendron tulipifera L. *Journal of Pharmaceutical Sciences*, *64*(5), 789-792.

11. Argui, H., Youchret-Zalleza, O. B., Suner, S. C., Periz, Ç. D., Türker, G., Ulusoy, S., ... & Said, H. (2021). Isolation, Chemical Composition, Physicochemical Properties, and Antibacterial Activity of Cupressus sempervirens L. Essential Oil. *Journal of Essential Oil Bearing Plants*, *24*(3), 439-452.

12. Zhang, Q., Tu, Q., Hickey, M. E., Xiao, J., Gao, B., Tian, C., ... & Wang, J. (2018). Preparation and study of the antibacterial ability of graphene oxide-catechol hybrid polylactic acid nanofiber mats. *Colloids and Surfaces B: Biointerfaces*, *172*, 496-505.

13. Sharma, S. K., Verma, D. S., Khan, L. U., Kumar, S., & Khan, S. B. (Eds.). (2018). *Handbook of materials characterization*. New York, NY, USA:: Springer International Publishing.

14. Yang, Z., Li, X., Si, J., Cui, Z., & Peng, K. (2019). Morphological, mechanical and thermal properties of poly (lactic acid)(PLA)/cellulose nanofibrils (CNF) composites nanofiber for tissue engineering. *Journal of Wuhan University of Technology-Mater. Sci. Ed.*, *34*, 207-215.

15. Cesur, S., Oktar, F. N., Ekren, N., Kilic, O., Alkaya, D. B., Seyhan, S. A., ... & Gunduz, O. (2020). Preparation and characterization of electrospun polylactic acid/sodium alginate/orange oyster shell composite nanofiber for biomedical application. *Journal of the Australian Ceramic Society*, *56*, 533-543.

16. Argui, H., Suner, S. C., Periz, Ç. D., Ulusoy, S., Türker, G., Ben-Attia, M., ... & Said, H. (2021). Preparation of cypress (Cupressus sempervirens L.) essential oil loaded poly (lactic acid) nanofibers. *Open Chemistry*, *19*(1), 796-805.
17. Qin, Y., Li, W., Liu, D., Yuan, M., & Li, L. (2017). Development of active packaging film made from poly (lactic acid) incorporated essential oil. *Progress in Organic Coatings*, *103*, 76-82.
18. Javidi, Z., Hosseini, S. F., & Rezaei, M. (2016). Development of flexible bactericidal films based on poly (lactic acid) and essential oil and its effectiveness to reduce microbial growth of refrigerated rainbow trout. *LWT-Food Science and Technology*, *72*, 251-260.

FTP-4

Electrodeposition Of CdS Thin Films at Various Cathodic Potential Values

Akın Keniş, Ayça Kıyak Yıldırım*

**Bilecik Şeyh Edebali University. Department of Motor Vehicles and Transportation Technologies. Bilecik Şeyh Edebali University.11210 Bilecik/Türkiye*
Bilecik Şeyh Edebali University. Department of Energy Systems Engineering Bilecik Şeyh Edebali University.11210 Bilecik/Türkiye

akinkenis@gmail.com, ayca.kiyakbilecik.edu.tr*

Abstract
The effects of cathodic potential on CdS thin films fabricated by using electrodeposition were investigated in detail. The cathodic potential values were adjusted between -0,55 V and -0,70 V. The structural, optical and morphological properties of the films were analyzed by using X-ray diffraction, ultraviolet-visible spectroscopy and scanning electron microscopy, respectively. Compact films with good crystallinity were obtained at the cathodic potential value of-0,60 V and -0,65 V. Ultraviolet-visible spectroscopy was used for estimating the energy band gap. The energy band gaps varied from 2,03 eV to 2,43 eV.

Keywords: Cadmium sulphide, CdS, Electrodeposition

Introduction

Cadmium sulfide (CdS) is an n-type semiconductor and has a direct optical band gap of about 2.2 eV to 2.6 eV at room temperature. II-VI group metal is known as chalgogenide semiconductor [1]. Surface morphologies of CdS thin films affect their optical properties. This is an important factor for the applications of photovoltaic devices. For this reason, morphology controlled CdS thin film production is technologically important [2, 3, 4]. CdS thin films, thermal evaporation [5], vacuum evaporation [6], chemical vapor deposition [7], electrodeposition [8, 9], RF sputtering [10], chemical spraying [4], sequential ionic layer adsorption and reaction (SILAR) [4], chemical bath storage [11, 4]. Among these methods, electrodeposition stands out as an attractive technique for the preparation of thin films in commercial quantities because it requires relatively inexpensive equipment, allows deposition over large areas, and is easy to control the growth parameters [12, 9].

Material and Method

In this study, CdS thin films were produced on ITO-coated glass substrates by using Chronoamperometer, one of the electrodeposition techniques. A three-electrode galvanostat/potentiostat device was used in the experiments. ITO is used as working electrode, saturated calomel electrode as reference electrode and platinum wire as counter electrode here. 0,1 M $CdCl_2$ and 0,1 M $Na_2S_2O_3$ were dissolved in 100 mL deionized water. The bath temperatures were kept at constant value of 80±2 °C. The solutions pHs were adjusted to 6,5. The experiments were completed in 2400 seconds. Electrochemical deposition system demonstrate in Figure1 was used all experiment. The depositions contexts are shortened in Table 1.



Figure 1: Electrochemical deposition system

Table 1: The deposition conditions of the CdS thin films

Experiments	Concentration of $CdCl_2$ (M)	Concentration of $Na_2S_2O_3$(M)	Deposition time (sec)	Cathodic Potential (V)	Deposition temperature (°C)	pH
D1	0,1	0,1	2400	-0,55	80± 2	6,5
D2	0,1	0,1	2400	-0,60	80 ± 2	6,5
D3	0,1	0,1	2400	-0,65	80± 2	6,5
D4	0,1	0,1	2400	-0,70	80± 2	6,5

The crystallographic properties were analyzed with a PANalytical empyrean X-ray diffractometer. The transmittance and band gaps of the films were investigated by using a JASCO V–530 double-beam uv-vis spectrophotometer. A Zeiss supra 40VP SEM was used to determine surface properties of the films.

The X-ray diffraction patterns of the films

When XRD patterns are examined, it is seen that CdS films can be produced in Figure 2 and Figure 3. It is shown in Figures 2 and 3 that all films produced have peak intensities belonging to the (002) planes. It is understood from Figure 2 that the peak intensity of the (002) plane of the CdS film produced using the -0,65 V value of the cathodic potential is very high. This peak is related to the Cubic structure. XRD analysis of CdS films produced using a cathodic potential of -0,70 V shows the presence of Cadmium and Sulfur peaks. In addition, it is seen that the films produced using the cathodic potential values of -0,55 v and -0,65 V have peaks belonging to the (111) plane. Film thicknesses were determined using the gravimetric method and all films have thicknesses in the range from 500 nm to 650 nm. It was observed that the thickness increased as the cathodic potential value used for the electrodeposition process increased.

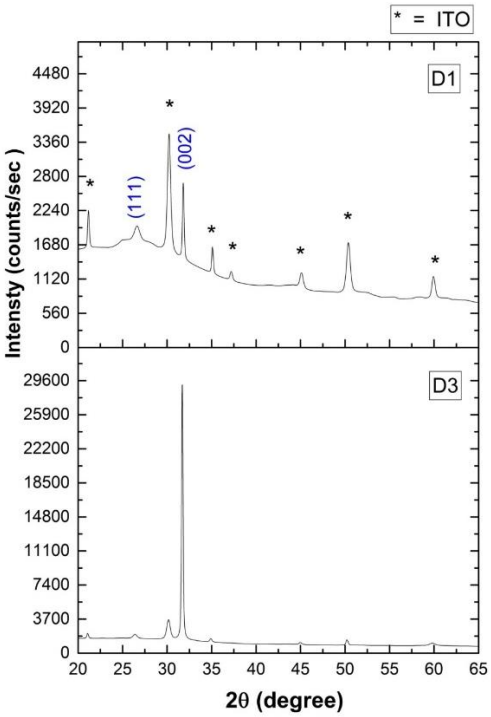


Figure 2

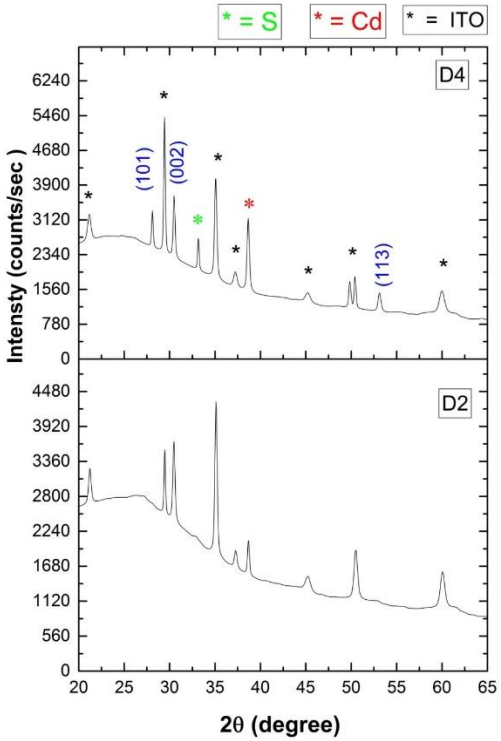


Figure 3

2.2. Optical properties of of the Films

The absorbance measurements versus wavelength were given in Figure4. The Tauc relation given in Equation 1was used to estimate energy band gaps.

$$\alpha h\upsilon = A(h\nu - E_g)^n \quad (1)$$

where hυ is photon energy, A is constant, Eg is optical band gap, n = for direct band gap material

and n = 2 for indirect band gap materials [13]. Figure 5 shows the Tauc plot of CdS films. By using this graph, the forbidden band gap of CdS films was calculated in the range of 2 to 2,43 eV. This value is in good agreement with the literature. The band gaps of the films were affected by the crystal size.

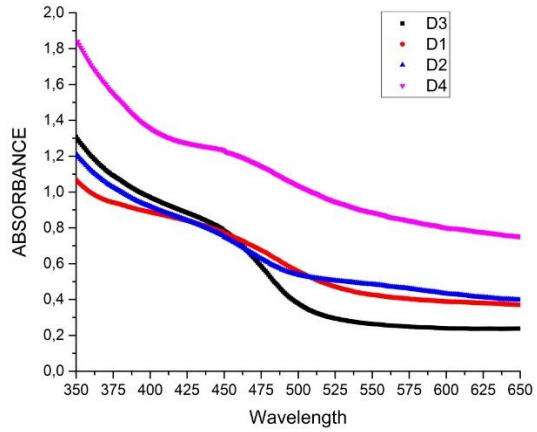


Figure 4 : The absorbance measurements of CdS films

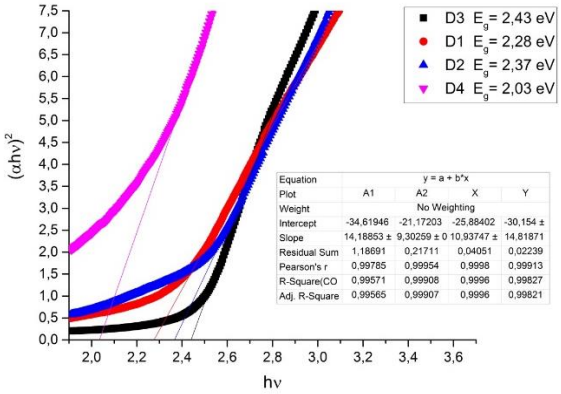


Figure 5 : The Tauc plot of CdS films

2.3 SEM images of the Films

SEM images of the films produced using -0,65 V and -0,70 V cathodic potential, at 30000 times magnification, are given in Figure 6 and Figure 7, respectively. It has been shown from the SEM images that the cathodic potential value has a great influence on the surface morphologies. The surface of the film obtained at -0,65 V is estimated to have relatively low surface roughnesses.

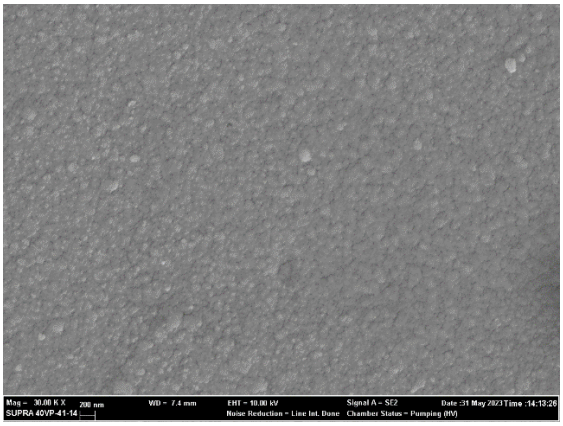


Figure 6: SEM images of the films produced using -0,65 V cathodic potential

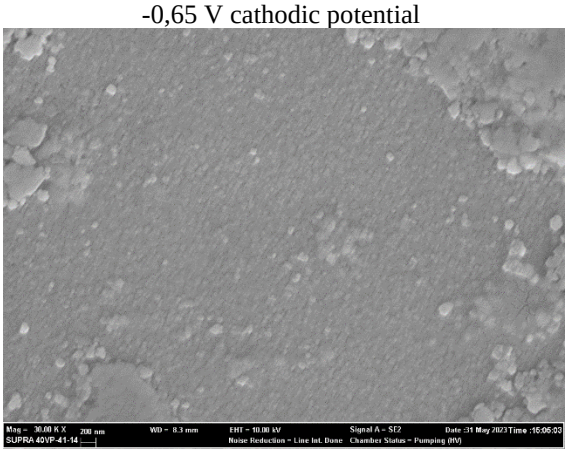


Figure 7 : SEM images of the films produced using -0,70 V cathodic potential

3. Conclusion

In this study, the effects of cathodic potential on electrodeposited CdS thin films were investigated. The XRD results showed that the peak intensity was predominantly high when the cathodic potential was -0,65 V. In addition, XRD results showed that all films formed in cubic crystal structure except the film produced at -0,70 V. The optical properties of the films were analyzed using absorbance measurements. It was observed that the film obtained by using a cathodic potential of -0,65 V showed high transmittance. It was concluded that low surface roughness and good crystallization may cause this result. The energy band gaps of the films range from 2 eV to 2,43 eV and are in agreement with the studies in the literature. As a result, in this study, it is thought that the films produced by keeping the experimental conditions constant and using the -0,65 V cathodic potential are more suitable for the solar cell sub-base.

4. References

Singh, T., Pandya, D. K., & Singh, R. (2011). Electrochemical deposition and characterization of elongated CdO nanostructures. *Materials Science and Engineering: B*, *176*(12), 945-949.

Kim, M.J., Kim, H.T. Kang, J.K., Kim, D.H., Lee, D.H., Lee, S.H., Sohn, S.H. (2010) Effects of the surface roughness on optical properties of CdS thin films, Molecular Crystals and Liquid Crystals, 532:1, 21/437-28/444. doi: 10.1080/15421406.2010.497099

Yücel E., Yücel Y., Durak M. (2016) Process optimization for window material CdS thin films grown by a successive ionic layer adsorption and reaction method using response surface methodology, Journal of Alloys and Compounds, 664, 530-537.doi: 10.1016/j.jallcom.2016.01.018

Yücel, E. (2017). Güneş Pili Uygulamaları İçin Cds İnce Filmlerin Optik Özelliklerinin Maltoz Katkısıyla Geliştirilmesi. Uludağ University Journal of The Faculty of Engineering, 22(2), 1-10.

Huang, L., Wei, Z.L., Zhang, F.M., Wu, X.S. (2015) Electronic and optical properties of CdS films deposited by evaporation, Journal of Alloys and Compounds, 648, 591-594. doi: 10.1016/j.jallcom.2015.07.041

He, Z., Zhao, G., Weng, W., Du, P., Shen, G., Han, G. (2005) The difference between the transverse and in-plane resistivity of vacuum evaporated cadmium sulfide (CdS) thin films, Vacuum, 79, 14-18. doi:10.1016/j.vacuum.2005.01.004

Uda, H., Yonezawa, H., Ohtsubo, Y., Kosaka, M., Sonomura, H. (2003) Thin CdS films prepared by metalorganic chemical vapor deposition, Solar Energy Materials and Solar Cells, 75, 219-226. doi:10.1016/S0927-0248(02)00163-0

Lu, C., Zhang, L., Zhang, Y., Liu, S., Liu, G. (2014) Fabrication of CdS/CdSe bilayer thin films by chemical bath deposition and electrodeposition, and their photoelectrochemical properties, Applied Surface Science, 319, 278-284. doi: 10.1016/j.apsusc.2014.08.158

Kıyak Yıldırım, A. (2018). Electrodeposition of CdS thin films under a magnetic field. *Materiali in tehnologije*, *52*(5).

Kim, M.J., Kim, H.T. Kang, J.K., Kim, D.H., Lee, D.H., Lee, S.H., Sohn, S.H. (2010) Effects of the surface roughness on optical properties of CdS thin films, Molecular Crystals and Liquid Crystals, 532:1, 21/437-28/444. doi: 10.1080/15421406.2010.497099

Yücel, E., Güler, N., Yücel, Y. (2014) Optimization of deposition conditions of CdS thin films using response surface methodology, Journal of Alloys and Compounds, 589, 207-212. doi: 10.1016/j.jallcom.2013.11.067

Singh, T., Pandya, D. K., & Singh, R. (2011). Annealing studies on the structural and optical properties of electrodeposited CdO thin films. *Materials chemistry and physics*, *130*(3), 1366-1371.

Vishwakarma, S. R., Tripathi, R. S. N., Verma, A. K., & Rahul. (2012). Study of n-type InSb thin films grown on glass substrate by electron beam evaporation technique. *Proceedings of the National Academy of Sciences, India Section A: Physical Sciences*, *82*, 245-249.

FTP-5

Charged Vector Boson Research with Ensemble Learning Techniques

Serpil Yalçın Kuzu*[a], and Ayben Karasu Uysal[b]

*[a] *Department of Physics, Fırat University, Elazığ, Türkiye*
[b] *Department of Physics, Yıldız Technical University, İstanbul, Türkiye*

Abstract

W bosons are electrically charged gauge bosons that mediate the weak force, which is responsible for important processes such as beta decay and neutrino interactions. These particles are quite massive, with a mass of around 80 GeV/c² and are produced in high-energy particle collisions. To study these particles, ensemble machine learning techniques can be applied to identify patterns and correlations in large datasets of high-energy particle collisions. In this talk, implementation of ensemble learning to W boson analysis is discussed focusing on challenges and opportunities of using machine learning. The results demonstrate the potential of ensemble learning in physics analysis.

1. Introduction

The W boson, one of the elementary particles predicted by the Standard Model of particle physics, is one of the significant probes for understanding the fundamental forces and elementary particles. As a carrier of the weak force, the W boson plays a crucial role in processes such as beta decay and neutrino interactions. Studying the properties and behaviors of the W boson provides valuable insights into the nature of the electroweak interaction [1]. The characteristic features of the boson are listed in Table 1 [2].

Table 1: Characteristic features of W Boson [2].

Mass (GeV/c^2)	80.377±0.012
Lifetime (s)	~3×10^{-25}
Charges	+/-1

The CMS (Compact Muon Solenoid) experiment at the Large Hadron Collider (LHC) at CERN, has been developed to understand characteristics of subatomic particles through high-energy collisions. In 2010, the CMS detector collected a rich dataset from proton-proton collisions at a center-of-mass energy of 7 TeV [3]. This dataset is available for various types of experimental measurements, providing a comprehensive view of the particles produced during the collisions.

Machine learning (ML) and artificial intelligence (AI) techniques are powerful tools in the field of particle analysis, revolutionizing the way to study particle physics. Particle physics experiments generate vast amounts of complex data requiring sophisticated analysis methods to extract meaningful insights. Machine learning algorithms offer a unique capability to automatically learn patterns, correlations, and intricate relationships within these datasets, enabling researchers to unravel the properties and interactions of particles more effectively. In this study, the W boson was analyzed with the ML model, which is Random Forest (RF) [4], by using the CMS 2010 proton-proton collision dataset. The performance of the algorithm was evaluated to classify events involving the W boson accurately.

1.1 Random Forest Classifier

The Random Forest (RF) [4] Classifier, one of the popular ensembles learning methods, has demonstrated high performance in various domains, including particle analysis. Ensemble learning refers to the combination of multiple individual models to make collective predictions, resulting in improved accuracy due to the reduction of the correlations. In RF, it constructs an ensemble of decision trees through bootstrap sampling and feature randomization, in which each tree independently contributes to the final prediction. The combination of these decisions reduces overfitting, overlearning, and enhances the generalization ability of the model.

Numerous studies have successfully applied the Random Forest Classifier in particle physics [5-7], demonstrating its ability to handle datasets and accurately classify particle interactions [8,9]. The model provides a robust framework for particle analysis, enabling reliable identification and characterization of particles within complex collision data.

2. Dataset Description and Model Implementation

The CMS 2011 proton-proton collision at a center-of-mass energy of 7 TeV dataset was used for the RF application to the W boson analysis [10, 11]. The dataset contains information about the decay products of the boson, electron (e^-), or positron (e^+) and the corresponding neutrino (ν_e). This information are run number, event number, transverse momentum of the electron (p_t), pseudorapidity of the electron, the angle of the electron direction, the charge of the electron, type representing electromagnetic calorimeter information of the electron, the difference in between the track and the cluster ($\Delta\varphi$), the difference in between the track and the cluster, the weighted cluster, the ratio of the energies stored in hadronic and electromagnetic calorimeter, the isolation variable for tracks, the isolation variable for the electromagnetic calorimeter, the isolation variable for the hadronic calorimeter, the missing transverse energy (MET)which is information of the neutrino, and missing energy angle. The primary objective is to classify events involving W bosons accurately by using the features in the dataset having discriminative power. For this purpose, ~405k events including electrons and neutrinos (ν_e) were analyzed. For the analysis an event was studied if there was one electron in the event with p_t>25 GeV and the event was rejected if there was a second electron present with p_t>20 GeV. The transverse mass of the was reconstructed by the equation represented below

$$M_t = \sqrt{2p_t MET(1-\cos(\Delta\varphi))} \qquad \text{Equation (1)}$$

and the distribution is represented in Figure 1. The events having W boson labeled as signal class similar to the particle physics analysis [12] including 89069 events. The rest of the dataset was considered as background. As a result, before the model implementation signal and background classes were defined. For the model application 70% of data was separated for training and the rest for the test.

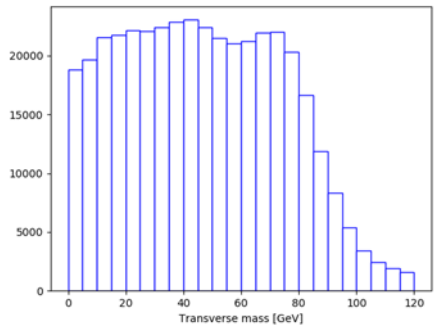


Figure 1. Transverse mass distribution of the dataset.

3. Model Performance Results

The performance of RF for event classification of W boson was assessed by metrics derived from confusion matrix which represents the success of ML model to find W boson events. An example of the confusion matrix is demonstrated in Figure 2. In the figure, true positive (TP) is the data belonging to the W boson signal which is correctly detected by the ML method; true negative (TN) represents the background correctly determined by the ML model; false negative (FN) indicates the signal detected as the background by the model, and (iv) false positive (FP) represents the data corresponds to the background which was identified as a boson signal by the model. In the ideal case, FP and FN values are expected to be 0.

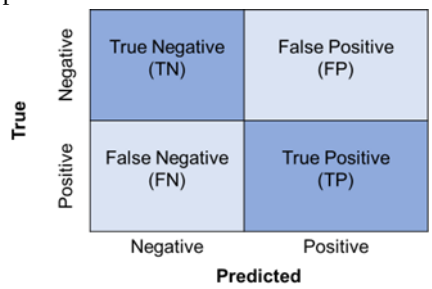


Figure 2. Confusion matrix.

ML evaluation metrics used in the analysis were selected as precision, recall, F-1 score, and ROC AUC [13] since the dataset is not highly imbalanced. Recall or sensitivity is the ratio of the signal correctly detected by the model in the dataset to the entire true signal class. It will be calculated as in Equation 2 using the parameters in the confusion matrix [14]. The precision represents the performance of the algorithm in detecting the signal presented in Equation 3 [14]. The F1 score, which

enables the evaluation of model performance by considering sensitivity and precision together, will be calculated with the harmonic mean as shown in Equation 4 [14]. ROC [13] was used to understand how well RF identified the boson events by using area information under the curve (ROC AUC). The values close to 1 indicate that the model has excellent performance.

$$\text{Precision}=TP/(TP+FP) \quad \text{Equation (2)}$$

$$\text{Recall}=TP/(TP+FN) \quad \text{Equation (3)}$$

$$\text{F-1 Score}=(2\times\text{Precision}\times\text{Recall})/(\text{Precision}+\text{Recall}) \quad \text{Equation (4)}$$

The metric values are represented in Table 2. ROC graph is demonstrated in Figure 3. The model identified W boson 99. 986% success with 99.248% precision and 99.267% sensitivity.

Table2. RF performance evaluation.

Model	Precision	Recall	F-1 Score
RF	0.99248	0.99267	0.99253

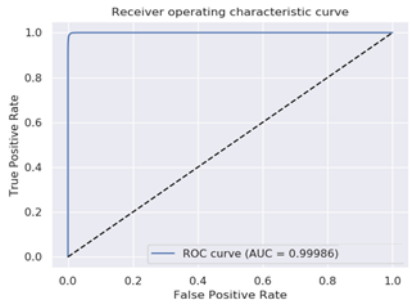


Figure 4. ROC curve of RF model.

4. Conclusions

The study demonstrates the application of the Random Forest Classifier to investigate the characteristics of the W boson using the CMS 2010 proton-proton collision dataset at √s=7 TeV. The application results highlight the classifier's ability to accurately identify W boson events, shedding light on the properties of the W boson in the algorithm implementation. This research contributes to the understanding of the performance of machine learning on particle physics analysis. In future studies, it is aimed to expand the analysis by incorporating more advanced machine learning techniques, such as deep learning models, to further improve the classification performance. Additionally, including data from more recent collision experiments will enable to explore the evolution of W boson characteristics with increasing energy.

Acknowledgments

This work is supported by the Scientific and Technological Research Council of Turkey (TUBITAK) project no 123F060.

References

1 MiniBooNE Collaboration, *Phys. Rev. Lett.*, 2013, **110**, 161801.
2 Particle Data Group, *Prog. Theor. Exp. Phys.*, 2022, 083C01.
3 CMS Collaboration, *Physics Letters B*, 2012, **716**, 30-61.
4 L. Breimen, *Machine Learning*, 2001, **45**, 5-32.
5 S. Yalcin Kuzu, *Eur. Phys. J. Plus*, 2022, **137**, 392.
6 S. Yalcin Kuzu, *Eur. Phys. J. Plus*, 2023, **138**, 41.
7 S. Yalcin Kuzu, *Journal of Scientific Computation*, 2023, **95**, 21.
8 C. Adam-Bourdarios, et al., *Journal of Physics: Conference Series*, 2014, **513**(3), 032005.
9 LHCb Collaboration, *JHEP*,2016, **05**, 81.
10 CMS. "Luminosity".https://twiki.cern.ch/twiki/bin/view/CMSPublic/LumiPublicResults#2010_proton_proton_7_TeV_collisi
11 CMS. "W boson data". https://opendata.cern.ch/record/5204
12 A. Tharwat, *Applied Computing and Informatics*, 2020, **17**.
13 A. P. Bradley, *Pattern Recognition*, 1997, **30**, 1145-1159.
14 F. Pedregosa, *Journal of Machine Learning Research*, 2011, **12**, 2825-2830.

FTP-6

Theoretical Computation of Structural and Electronic Structure Properties of Metal Halide Perovskite $CsSnBr_3$: A DFT Study

Merve Ozcan*[1], F. Hayal Gecit[2], Suleyman Cabuk[2]

[1]*Electric-Electronic Engineering, Toros University, Faculty of Engineering, Mersin, Türkiye*

[2]*Physics Department, Çukurova University, Faculty of Sciences and Letters, Adana, Türkiye*

*merve.ozcan@toros.edu.tr

We calculated the structural and electronic properties of $CsSnBr_3$ in the cubic structure. The calculations of $CsSnBr_3$ structure were performed for unit cell and supercell (2×2×2) with 40 atoms. Also, the supercell of $CsSnBr_3$ by replacing one Sn atom by one Ni atom was obtained. First of all, the lattice parameters were determined by geometric optimization. We also obtained bond lengths and electronic band structure, total density of states (DOS) and partial density of states (PDOS) of the structures using geometrically optimized structures. All calculations were performed using Vienna Ab Initio Simulation Package (VASP) code with ab-inito method based on standard Density Functional Theory (DFT). The generalized gradient approach (GGA) within the Perdew-Wang (PW91) scheme was applied to treat the exchange-correlation fucntion. We compared our results with other available theoretical and experimental results.

Keywords: Sn-based perovskite, structural, bond length, electronic structure, DFT

1.Introduction

Recently, metal halide perovskites have been attracted instead of lead (Pb)-based perovskite for solar cell and optoelectronic applications in the theoretical and experimental research. Metal halide perovskites which exhibit excellent properties like Pb-based perovskites because of environmentally problems and toxicity which is caused by Pb. Thus, the researchers have focused halide perovskite instead of Pb-based perovskite. This perovskite group have been attracted are widely studied in solar cell and optoelectronic applications [1]. Perovskites semiconducting materials have an important role on the progress of the third-generation photovoltaic cells. Thus, the solar cell based on perovskites have been attracted in experimental and theoretical studies because of excellent physical and chemical properties. The tunable electronic band gap is the most important advantage of the perovskites [2]. Typically structure of perovskites with chemical formula ABX_3 have unit cell that includes five atoms in a cubic structure. While A and B represent cation, X refers to I, Cl, Br and F with halogen group. The Goldschmidt tolerance factor should be close to 1 for cubic structure because of protect of high-symmetry structure [3]. Pramchu et al. studied $CsSnBr_3$ electronic properties using DFT with GW method for more accurate electronic band gap. They reported its band gap is suitable for solar cell applications. Although the electronic band structure of cubic $CsSnBr_3$ has been widely studied by several groups, it is relatively unknown is compared to tetragonal and monoclinic phase. Zheng et al. focused the electronic properties of $CsSnBr_3$ using experimental and theoretical method. They reported that $CsSnBr_3$ has a narrow-band gap. It exhibits semiconductor behavior characterization with band gap near the Fermi level. Also, they calculated that the conduction band and valance band changed with phase transition which occurred from a cubic phase to tetragonal phase [4].

2. Computational details

In this work, we calculated the effect on structural and electronic properties of metal (Ni) dopant in $CsSnBr_3$.The supercell (2×2×2) which contain 40 atoms were obtained for $CsSnBr_3$ and Ni-doped CsSnBr3 structure. We calculated the structural and electronic properties of $CsSnBr_3$. Firstly, lattice parameters of unit cell structure and the supercell of $CsSnBr_3$ by replacing one Sn atom by one Ni atom were obtained using geometric optimization. The one Sn atom replacing by Ni atom correspond to 12.5 % concentration. The supercell (2×2×2) which contain 40 atoms were obtained for $CsSnBr_3$ and Ni-doped $CsSnBr_3$ structure. All calculations were performed using VASP code [8,9] based on DFT. The GGA within the PW91 scheme was applied to treat the exchange-correlation function. The cutoff

energy was 620 eV, 500 eV and 500 eV for unit cell, supercell and Ni-doped supercell, respectively. The Monkhorst-Pack scheme of 5×5×5 was taken for all structures.

3. Structural Properties

3.1. $CsSnBr_3$ structural properties

$CsSnBr_3$ is a cubic face-centered cubic structure with space group Pm-3m (No: 221). The structure contains five atoms in unit cell. There is one Cs atom, one Sn atom and 3 Br atoms. The Wyckoff positions are 1*a* (0,0,0) fractional coordinates, 1*b* (0.5, 0.5, 0.5) and 3*c* (0, 0.5, 0.5) for Cs, Sn and Br atoms, respectively.

Table 1. The lattice parameters (*a*/Å), volume (V_0/Å^3) of $CsSnBr_3$.

Structure	***a***	***V_0***
Unit cell	5.873, 5.802[a], 5.608[b], 5.804[c]	202.576, - (Calc., GW), 204[b] (Calc., GGA), 196 (Exp.)
Supercell	11.758	1625.835
Ni-doped supercell	11.746	1620.6103

[a][2], [b][5], [c][6],

The unit cell, supercell (2×2×2) and the supercell of $CsSnBr_3$ by replacing one Sn atom by one Ni atom are given Figure 1. The supercell (2×2×2) includes that 8 Cs atoms, 8 Sn atoms and 24 Br atoms, totally 40 atoms. All images were visualized using VESTA program [7].

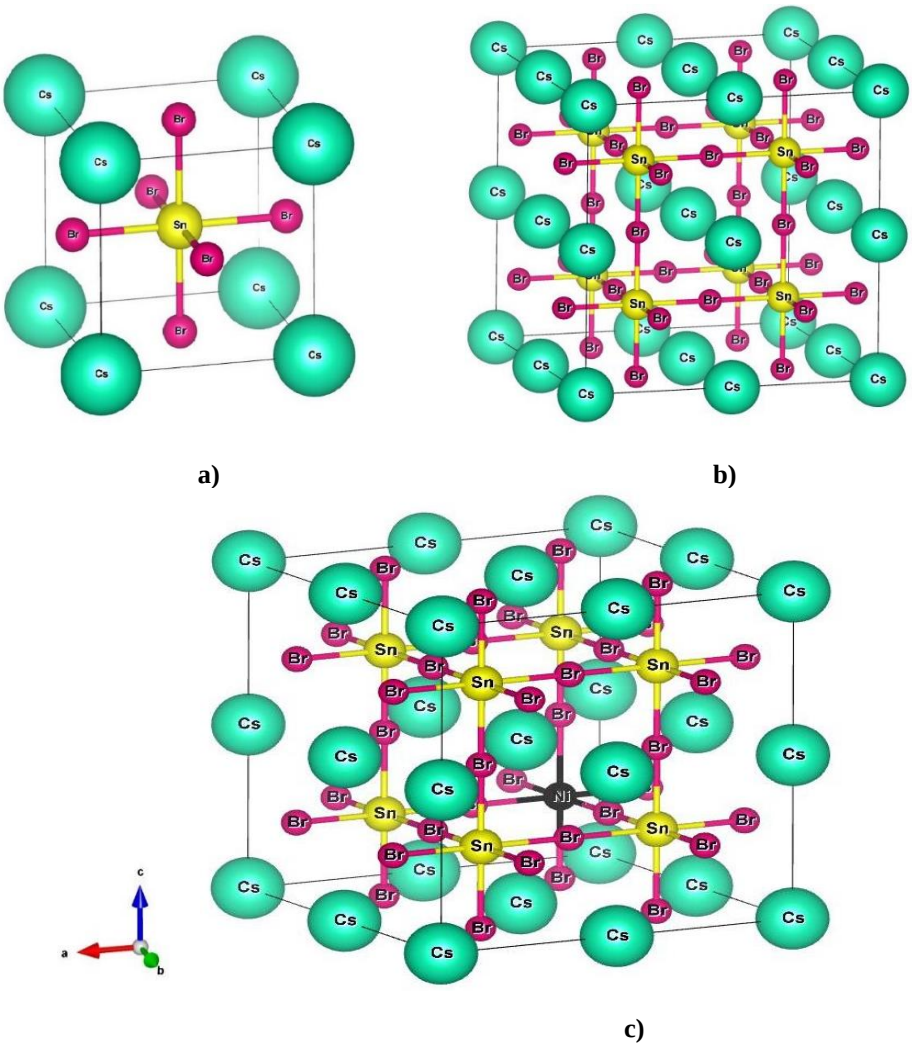


Figure 1. Crystal structure of $CsSnBr_3$ **a)** unit cell **b)** supercell (2×2×2) with 40 atoms **c)** Ni-doped of supercell (2×2×2) with 40 atoms

3.2. $CsSnBr_3$ bond lengths

ABX_3 type perovskite can be categorized in organic-inorganic halide perovskites an all-inorganic halide perovskite [15]. In this structure, B is bonded to six X halogen ions. Thus, BX_6 octahedra form with corner-connected occur [17]. The chemical composition determines the crystal structure and stability of perovskite. In ABX_3 chemical formula, A is a cation and B is a metal ion, X is halogen. Li et al. reported that the halide ions passing through from I, Br, Cl and F, the electronegativity increases, and the ionic radius is smaller. It refers that increasing the chemical bonding between halide ions and cations with A and B [16]. We calculated that Cs-Br, Cs-Cs and Br-Sn bond lengths. Table 2 shows that these calculated bond lengths.

Table 2. The calculated bond lengths (Å) of $CsSnBr_3$

Structure	***Cs-Br***	***Cs-Cs***	***Br-Sn***
Unit cell	4.152 4.162[a]	5.873 5.886[a]	2.936 2.943[a]
Supercell	4.157	5.879	2.939
Ni-doped supercell	4.152	5.873	2.936

[a][1]

Hossain et al. reported that interaction between B and X with Cl, Br and I ion group is directly affect the band gap of halide perovskite. Also, A cation don't directly affect the band gap. The covalent interactions between Sn and X becomes stronger from I to Br, then to Cl because of the bond length between Sn and X decrease passing Cl to Br, then to I [17].

4. Electronic band structure

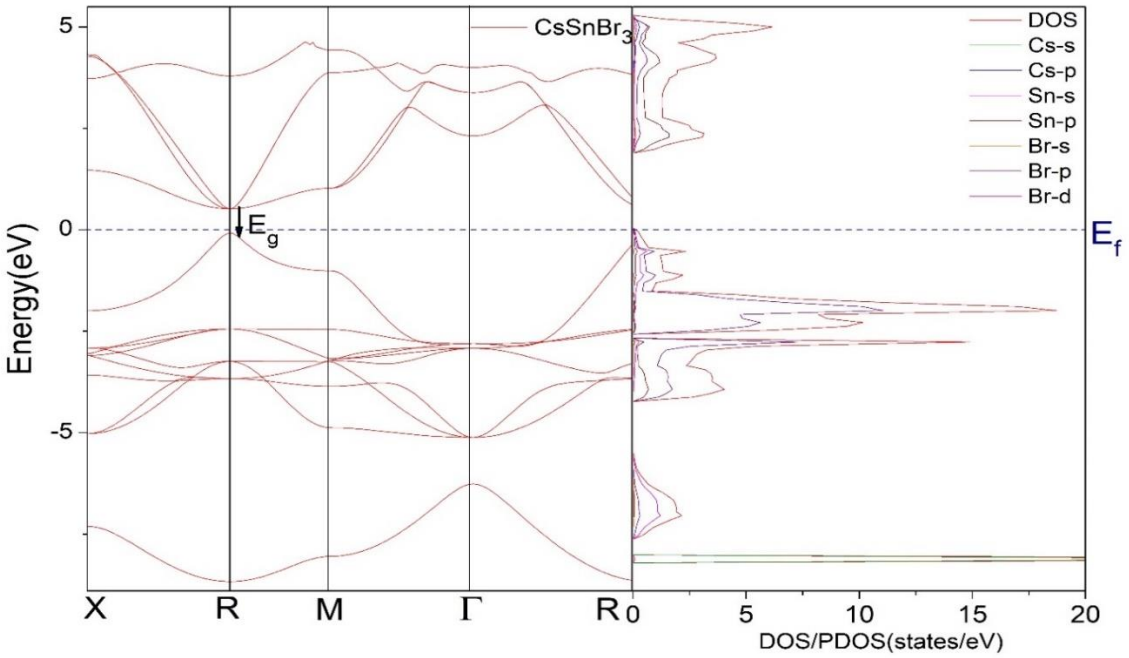
4.1. $CsSnBr_3$ electronic band structure and density of states (DOS)

The experimental and theoretical studies show that the most effective way to improve the optical and electronic properties of all-inorganic halide perovskites is doping metal. Especially, rare earth dopants on the Pb site have exhibit excellent optoelectronic properties. The band which is close to Fermi level is relationship with physical performance of the material [10]. The electronic band structures of $CsSnBr_3$ compound were calculated using PW91 function along the high symmetry points (X - R - M - Γ- R). The high symmetry points in reciprocal lattice at Brillouin Zone of $CsSnBr_3$ compound was calculated for cubic structure. The calculated electronic band gaps (E_g) of $CsSnBr_3$ are given Table 3.

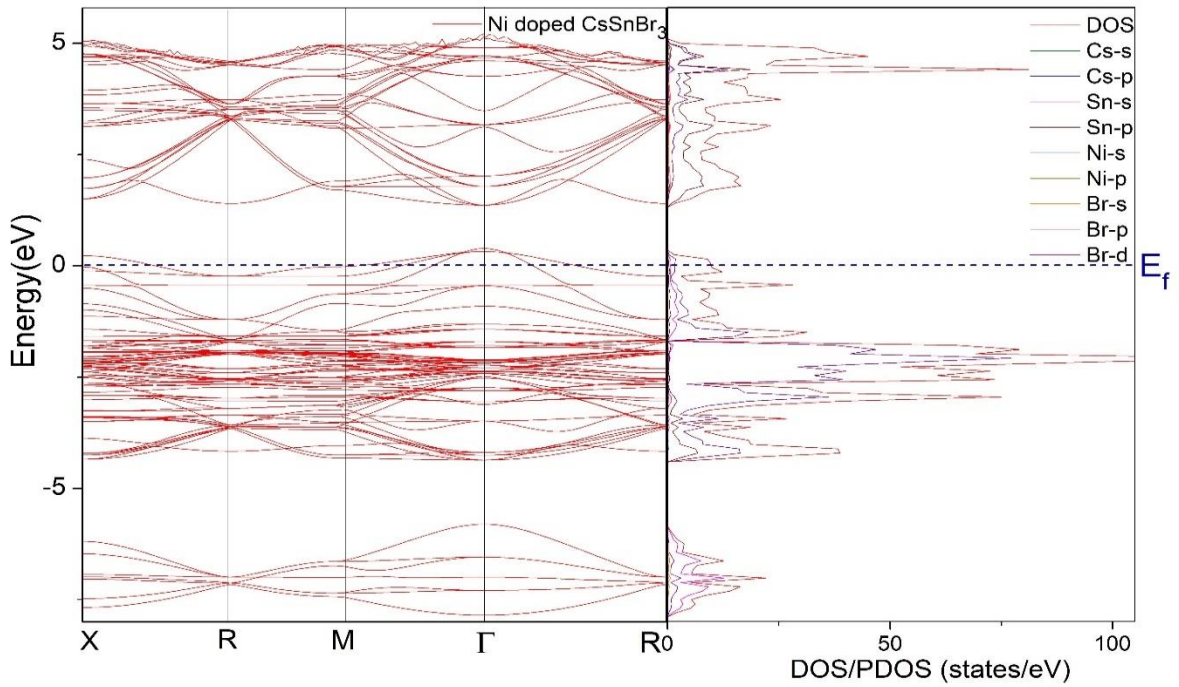
Table 3. The electronic band gap of $CsSnBr_3$ structure

Structure	*E_g (eV)*
Unit cell	0.597, 0.58[a], 0.35[b], 0.630[c], 0.62[d]
Supercell	0.594
Ni-doped supercell	Metallic, 0.16[e]

[a][11], [b][12], [c][13], [d][14], [e][10]



a



b

Figure 2. Electronic structure and DOS of $CsSnBr_3$ a) unit cell, b) Ni-doped supercell

It was found that the direct electronic band gaps (E_g) are at point R and Γ for unit cell and supercell, respectively. The Fermi level (E_f) is illustrated as dashed line in Fig. 2. We observed that the valance band exceed the Fermi level for Ni-doped supercell. Its mean that Ni-doped $CsSnBr_3$ exhibits metallic behavior. It can be concluded that metal dopant is one of the important methods for improving electronic band structure. Also, we calculated DOS and PDOS for detailed understanding electronic band structure. As it seen DOS and PDOS graphs, the sharp peak was observed about -2.5 eV in valance band for all structures. Also, the hybridization was observed in this region. Tang et al. focused on the structural stability and optoelectronic properties of $CsSnBr_3$ compound. The maximum point of valance band and minimum point of conduction band are located at point Γ of the Brillouin Zone. Also, the weak hybridization between *Sn-p* and *Br-p* orbitals was reported at -5 eV and -3 eV. They reported that band gap of Ni, Zn and Cd-doped structure transition from the direct band gap to an indirect band gap. Also, Ni-doped $CsSnBr_3$ structure exhibits half-metal behavior. The band gap of Ni-doped $CsSnBr_3$ was reported 0.16 eV. While they calculated that the expanding band gap with doping Mn, Cr and Cu dopants in $CsSnBr_3$ structure [10]. Ye et al. reported that the different halogen changes the positions of valance band maximum and conduction band minimum. Also, the valance band maximum of $CsSnBr_3$ is higher than $CsSnCl_3$ and $CsSnI_3$ [17]. Li et al. reported that B site metal and X-site halogen ion directly effect the band gaps of the ABX_3 type perovskite [13]. Hosaain et al. studied on the optoelectronic properties of $CsSnBr_3$ perovskite under hydrostatic pressure. They focused on the relationship between bond length and electronic band structure. They reported that $CsSnBr_3$ exhibit metallic characterization, when the bond lengths reach a certain value under hydrostatic pressure [1].

4. Conclusions

In this study, we aimed to calculate the structural and electronic properties of unit cell, supercell and also Ni-doped supercell of $CsSnBr_3$ with cubic structure. Especially, we investigated the effect of metal (Ni) dopant on the structural and electronic band gap of the $CsSnBr_3$. We created supercell for doping of the metal dopant on the $CsSnBr_3$ structure by replacing one Sn atom replacing by Ni atom. Lattice parameters and band gap, DOS and PDOS were calculated of all structures at ambient pressure. We observed that calculated bond lengths are similar to both unit cell and supercell structure. The band structure of unit cell a direct band gap reveals at point (R→R). While unit cell structure exhibit semiconductor behavior with narrow-band gap, Ni-doped supercell structure exhibits metallic behavior. It was observed that valance band exceed the Fermi level for Ni-doped $CsSnBr_3$. From the DOS and PDOS graphs of all structures, the sharp peaks were observed about 5 eV in conduction band and about -2.5 eV in valance band. It can be concluded that it is

one of the important methods of the improving of the band structure is metal dopant for the host material.

References

[1] Hossain Md. S., Babu Md. M. H., Saha T., Hossain Md. S., Podder J., Rana Md. S., Barik A., Rani P. 2021. Pressure induced semiconductor to metal phase transition in cubic $CsSnBr_3$ perovskite. AIP Advances 11, 055024.

https://doi.org/10.1063/5.0048979

[2] Pramchu S., Laosiritaworn Y., Jaroenjittichai A. P., 2016. Electronic properties of surface/bulk iodine defects of $CsSnBr_3$ perovskite. Surface & Coatings Technology 306, 159-163.

https://doi.org/10.1016/j.surfcoat.2016.05.062

[3] Yin W-J., Yang J-H., Kang J., Yan Y., Wei S-H. 2014. Halide perovskite materials for solar cells: a theoretical review. Journal of Materials Chemistry A.

https://doi.org/10.1039/c0xx00000x

[4] Zheng J-C., Huan C. H. A., Wee A. T. S., Kuok M. H., 1999. Electronic properties of CsSnBr3: studies by experiment and theory. Surface and Interface Analysis 28, 81-83.

https://doi.org/10.1002/(SICI)1096-9918(199908)28:1<81::AID-SIA623>3.0.CO;2-D

[5] Kholil M. I., Bhuiyan M. T. H. 2021. Effects of pressure on narrowing the band gap**,** visible ligh absorption, and semi-metallic transition of lead-free perovskite CsSnBr3 for optoelectronic applications. Journal of Physics and Chemistry of Solids 154, 110083.

https://doi.org/10.1016/j.jpcs.2021.110083

[6] Barrett J., Bird S. R. A., Donaldson J. D., Silver J., 1971. The mössbauer effect in tin (II) compounds. Part XI. The spectra of cubic trihalogenostannates (II). Journal of the Chemical Society A: Inorganic, Physical, and Theoretical Chemistry 3105-3108.

https://doi.org/10.1039/J19710003105

[7] Momma K. And Izumi F. 2011. VESTA 3 for three-dimensional visualization of crystal, volumetric and morphology data. Journal of Applied Crystallography 44, 1272-1276.

https://doi.org/10.1107/S0021889811038970

[8] G. Kresse, J. Furthmuller. Efficient iterative schemes for ab initio total-energy calculations using a plane-wave basis set. Phys. Rev. B 54 (1996) s11169-11186.

https://doi.org/10.1103/PhysRevB.54.11169

[9] G. Kresse**,** J. Furthmuller. Efficiency of ab-initio total energy calculations for metals and semiconductors using a plane-wave basis set. Comput. Mater. Sci. 6 (1996) s15-50.
https://doi.org/10.1016/0927-0256(96)00008-0

[10] Tang F., Yao Y., Cao D., Yan J., Wang J., Jiang Z., Zhou Y., Jiao Z., Shu H. 2022. Structural stability and optoelectronic properties of elad-free halide perovskite $CsSnBr_3$ by introducing transition-metal dopants. Journal of Electronic Materials 51: 3438-3444.
https://doi.org/10.1007/s11664-022-09609-4

[11] Hossain Md. S., Babu Md. M. H., Saha T., Hossain Md. S., Podder J., Rana Md. S., Barik A., Rani P. 2021. Pressure induced semiconductor to metal phase transition in cubic $CsSnBr_3$ perovskite. AIP Advances 11, 055024.

https://doi.org/10.1063/5.0048979

[12] Pramchu S., Laosiritaworn Y., Jaroenjittichai A. P., 2016. Electronic properties of surafce/bulk iodine defects of $CsSnBr_3$ perovskite. Surface & Coatings Technology 306, 159-163.

http://dx.doi.org/10.1016/j.surfcoat.2016.05.062

[13] Liu Y., Yan W., Zhu H., Tu Y., Guan L. 2022. Study on bandgap predications of ABX_3-type perovskite by machine learning. Organic Electronics 101, 106426.

https://doi.org/10.1016/j.orgel.2021.106426

[14] Qian J., Xu B., Tian W. 2016. A comprehensive theoretical study of halide perovskites ABX_3. Organic Electronics, 37, 61-73.

https://doi.org/10.1016/j.orgel.2016.05.046

[15] Saad M. M., Yousif S. E. A. 2022. Structural and optoelectronic properties of CsSnBr3 metal halide perovskite as promising materials toward novel-generation optoelectronics. Chalcogenide Letters 19, 2, 153-162.

https://doi.org/10.15251/CL.2022.192.153

[16] Li N. Tao S., Chen Y., Niu X., Onwudinanti C. K., Hu C., Qiu Z., Xu Z., Zheng G., Wang L., Zhang Y., Li L., Liu H., Lun Y., Hong J., Wang X., Liu Y., Xie H., Gao Y., Bai Y., Yang S., Brocks G., Chen Q., Zhou H. 2019. Cation and anion immobilization through chemical bonding enhancement with fluorides for stable halide perovskite solar cells. Nature Energy, 4, 408-415.

https://doi.org/10.1038/s41560-019-0382-6

[17] Ye Y., Run X., Hai-Tao X., Feng H., Fei X., Lin-Jun W. 2015. Nature og the band gap of halide perovskites ABX_3 ($A=CH_3NH_3$, Cs; B=Sn, Pb; X=Cl, Br, I): First principles calculations. Chinese Physics B, 24, 11, 116302.

https://doi.org/10.1088/1674-1056/24/11/116302

FTP-7

Evaluation of Structural, Morphological and Electrical Properties of $Bi_4Sb_{38}Te_{58}$ Thin Film on Si(100)

Gizem Durak Yüzüak[1], Mehmet Çetin[2], and Ercüment Yüzüak[2,*]

[(1)] *Munzur University, Rare Earth Elements Application and Research Center, Tunceli, Türkiye*

[(2,*)] *Recep Tayyip Erdoğan University, Faculty of Engineering and Architecture, Rize, Türkiye*

*ercument.yuzuak@erdogan.edu.tr

Thin films with moderate thermoelectric properties are utilized in energy harvesting, solid-state cooling, and thermoelectric generators due to their ability to directly convert heat into electrical energy. The application of heat treatment has been found to enhance the thermoelectric properties of thin films, and the regulation of thin film annealing temperature together with surface microstructure is of paramount importance in energy harvesting. In the present study, the technique of magnetron sputtering was employed to fabricate thin films of Bi-Sb-Te, a widely recognized thermoelectric material, on Si(100) substrates. Subsequently, the thin films underwent annealing at a temperature of 250°C for a duration of 1 hour within a high vacuum environment characterized by a pressure of $2x10^{-5}$ mTorr. The thin film structure was evaluated using X-ray diffraction (XRD), scanning electron microscopy (SEM), and atomic force microscopy (AFM) measurements [2]. The measurement of electrical resistivity was conducted on thin films within the temperature range of room temperature (RT) to 250 °C. The electrical conductivity of crystalline thin films was enhanced through the process of vacuum annealing. After undergoing heat treatment at ambient temperature, the electrical resistivity of the power factor in the thermoelectric phenomenon, which quantifies a material's capacity to convert heat into electricity, exhibited a notable increase of approximately threefold. The results of this study indicate that the implementation of a Bi-Sb-Te thin film on a rigid Si(100) substrate as an energy harvesting device has the potential to enhance the efficiency of thermoelectric energy generation. The research places significant emphasis on enhancing the annealing temperature and surface microstructure of thin films in order to enhance their thermoelectric performance. This has far-reaching implications for applications related to energy conversion and heat management.

Introduction

Novel environmentally friendly energy sources, such as thermoelectricity, triboelectricity, piezoelectricity, pyroelectricity, etc., have been the focus of study in response to the energy problem and global warming [1-4]. Among the many types of emerging energy materials, thermoelectric technologies stand out for their unique ability to directly transform heat into electricity. Thermoelectric devices are advantageous because they do not pollute the environment, last a long time, require little to no maintenance, and have a high degree of dependability. A wide variety of sensors, air conditioners, and heat exchangers employ it. At room temperature (RT), the best thermoelectric characteristics are seen in the combination $Bi_xSb_{2-x}Te_3$ ($0<x<2$), often known as bismuth antimony telluride [4, 5]. Low-dimensional materials such as thin films have been the subject of intensive study in recent decades [6-9] with the result showing significant improvements in the thermoelectric characteristics of materials compared to their higher-dimensional counterparts. While this is happening, the demand for miniaturization may be met with the aid of thin film thermoelectric materials. As a result of its potential for large-scale production of superior films, magnetron sputtering was adopted as the development technique of choice. The best thermoelectric performance may be attained in bismuth telluride (BiSbTe) thin films by maintaining a stoichiometric ratio of [BiSb] to [Te]. Single target sputtering and varying sputtering capabilities of BiSbTe targets have been widely employed in studies to fine-tune compositions.

Exploring novel methodologies to effectively engender bulk-like thermoelectric properties in thin films in a manner that emulates the volumetric attributes of their bulk analogue constitutes a formidable challenge at the forefront of solid-science research. Developing high-performance

thermoelectric thin films at room temperature is critical for numerous applications and is a subject of ongoing research. Heat-treated Bi-Sb-Te thin films with a thickness of ~50 nm on rigid substrates have shown promising potential for achieving these desirable properties. In this work, thermoelectric performance can be significantly enhanced by optimizing the annealing temperature and surface microstructure, ultimately improving the energy-harvesting capabilities of these materials. To analyze the structural, morphological, and electrical properties of heat-treated $Bi_4Sb_{38}Te_{58}$ thin films investigated through X-ray diffraction, scanning electron microscopy, atomic force microscopy, and resistivity measurements, in the following steps, the analysis will be conducted to investigate the impact of vacuum annealing on the enhancement of electrical conductivity. Subsequently, an evaluation will be undertaken to explore the resulting improvements in power factor performance, thereby demonstrating the potential utilization of these materials in the field of thermoelectric energy generation. The analysis of these results will be conducted to determine their relevance in the context of enhancing high-performance thermoelectric devices, as well as their potential impact on the environment and economy. To improve the efficiency of waste heat utilization for power generation and promote the development of sustainable energy solutions, it is imperative to optimize both the annealing temperature and surface microstructure. This optimization process allows us to harness waste heat more efficiently, reducing our dependence on conventional energy sources. This study's main goal is to lay the groundwork for thermoelectric material advancements and their practical applications in real-world scenarios.

Materials and Methods

A thermoelectric thin film of $Bi_4Sb_{38}Te_{58}$ was deposited at room temperature on a Si(100) substrate using a single-target sputtering method. There is just one circular target and one RF power source in this magnetron sputtering system. As is well-known, magnetron sputtering offers several scientific advantages, including large output with fewer contaminants and simplified manipulation. In this study, a magnetron sputtering process was employed using a target with a diameter of 50 mm. The target material was a single piece of high-purity Bi-Sb-Te alloy with a purity of 99.9%. Before the deposition process, the substrates underwent a thorough cleaning procedure. Firstly, they were washed in deionized water, followed by immersion in an ultrasonic bath containing alcohol for 10 minutes. These cleaning steps ensure the removal of impurities and contaminants from the substrate surface. To create the desired composition of 4-38-58, the deposition chamber was evacuated to a pressure of 2 x 10^{-5} mTorr. During the sputtering process, Ar was introduced into the chamber at a flow rate of 30 sccm. The working pressure was maintained at a constant value of 5 mTorr. This controlled environment allows for precise control over the sputtering process and facilitates the desired composition. To enhance the uniformity of the deposition, the substrate holder was set to rotate at a speed of approximately 12 rpm. This rotation aids in achieving a more uniform deposition across the substrate surface.

To determine the chemical formula of elemental concentrations, energy-dispersive X-ray spectroscopy (EDX) data were collected and analyzed. The determined mean concentrations were found to be within 1 at.% of the expected nominal values. This level of accuracy demonstrates the effectiveness of the magnetron sputtering process in achieving the desired composition. Furthermore, SEM/EDX scans were conducted to validate the random distribution of components at the microscopic level. These scans provide visual confirmation that the components of the deposited film are uniformly distributed throughout the substrate surface, ensuring the desired properties and performance of the deposited material. Magnetron sputtering with a high-purity Bi-Sb-Te target offers significant advantages, such as large output with minimal contaminants and simplified manipulation. Through careful control of the deposition parameters and thorough cleaning of the substrates, the sputtering process yields precise compositions, validated by EDX analysis and SEM micro-imaging. This scientific approach enables the production of high-quality thin films with controlled compositions for various applications.

The AFM measurements were performed in tapping mode, which is a non-destructive mode that can be used to measure the topography of films. The AFM measurements were performed at a scan rate of 1 Hz, which is a slow scan rate that allows for high-resolution imaging, and in air, which is a common environment for thin-film devices. A four-point probe system was used to measure the electrical resistance of thin films of thermoelectric materials in a vacuum atmosphere. The four-point probe system was capable of measuring between room temperature and a 250°C baseline pressure of about 5×10^{-5} Torr using a turbomolecular pumping unit. The high temperature resistivity measurement ($\rho(T)$) was performed on the basis of the general four-point probe method. The $\rho(T)$ system had a current operating range of 100 fA to 100 mA (Keithley, 6221) and a measuring voltage of 10 nV to 12 V (Keithley, 2182A/E).

Results and Discussion

To gain further insights into the alloy BiSbTe target, scanning electron microscopy (SEM) was utilized, and images obtained from this technique are represented in Fig.1. According to Fig.1a, the surface of the bulk alloy to be used as the target has been found to have an almost homogeneous distribution. Additionally, an energy-dispersive X-ray spectroscopy (EDX) analysis was performed on the target, providing a spectrum that reveals the elemental composition. Figure 1b displays the EDX analysis of the alloy, accompanied by the corresponding elemental mapping. The results obtained from the study provide evidence that the alloy meets the initial specifications. Additionally, the results indicate the absence of any localized buildup of elements.

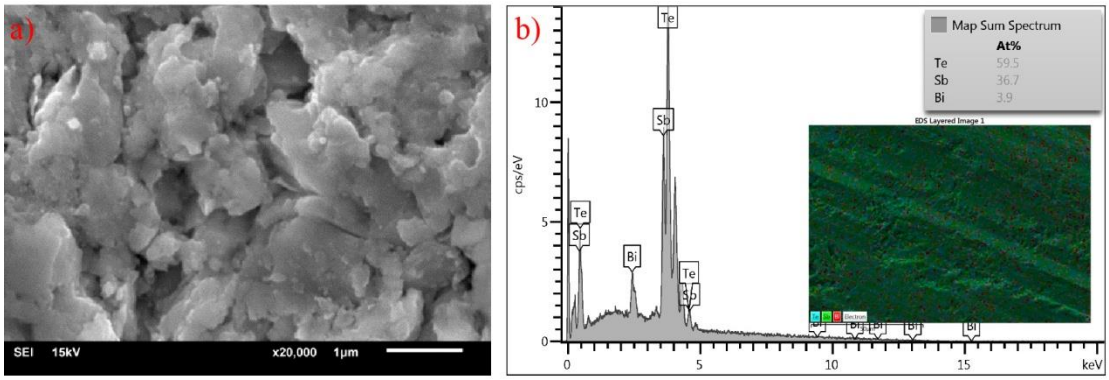


Fig 1. BiSbTe alloy target a) SEM image and b) EDX energy spectrum of image with the inset of elemental mapping

The structural experimental investigation involves the examination of BiSbTe-based thin films both before and after heat treatment. X-ray diffraction (XRD) patterns were obtained to analyze the crystalline structure of the films. The XRD patterns, presented in Fig. 2, were carefully analyzed to extract valuable information about the films' structural characteristics. Prior to heat treatment, the XRD patterns revealed that the films exhibited diffraction peaks corresponding to the R-3m space group. This space group indicates a rhombohedral crystal structure, which is consistent with the expected crystal structure of BiSbTe-based materials. The presence of well-defined diffraction peaks in the XRD patterns indicates that the films possess a considerable degree of crystallinity. Following the heat treatment process, an intriguing observation was made. The XRD patterns of the films after heat treatment exhibited narrower peak widths compared to the patterns obtained before heat treatment. This phenomenon suggests that the heat treatment led to an improvement in the crystalline quality of the films. The reduction in peak widths can be attributed to several factors. Firstly, the heat treatment process may have facilitated the removal of defects, such as vacancies or grain boundaries, which can introduce structural disorder and broaden the diffraction peaks. As a result, the narrower peak widths indicate a reduction in the presence of such defects, leading to an enhancement in the overall crystalline quality of the films. Moreover, the heat treatment process may have induced a partial recrystallization or rearrangement of the film's atomic structure. This recrystallization process can result in larger and more coherent crystalline domains, thereby leading to sharper and narrower diffraction peaks in the XRD patterns. The observed improvement in the crystalline quality of the films after heat treatment is of significant importance [10-12].

A higher degree of crystallinity generally correlates with improved electrical properties in thermoelectric materials. Therefore, the narrower peak widths in the XRD patterns indicate a potential enhancement in the thermoelectric performance of the BiSbTe-based thin films. It is worth noting that a more detailed analysis, such as peak broadening analysis using the Scherrer equation or further characterization techniques like transmission electron microscopy (TEM), could provide quantitative information about the crystallite size, lattice strain, and microstructural changes induced by heat treatment. The XRD analysis of the BiSbTe-based thin films revealed that they were predominantly crystallized in the R-3m space group. After heat treatment, a noticeable improvement in the crystalline quality was observed, as evidenced by the narrower peak widths in the XRD patterns. This improvement suggests a reduction in defects and a potential enhancement in the thermoelectric performance of the films. Further investigations and complementary characterization techniques can provide deeper insights into the microstructural changes induced by heat treatment, facilitating a more comprehensive understanding of the film's structural properties and their correlation with its thermoelectric behavior.

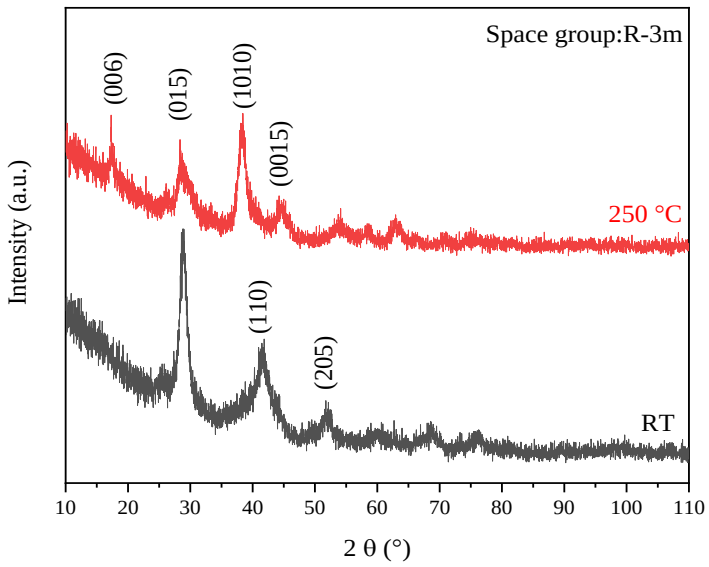


Fig 2. XRD patterns of room temperature deposited and high-vacuum annealed at 250°C thin films

In addition to the observed changes in peak widths, the examination of specific hkl planes in the XRD patterns provided further insights into the structural evolution of the BiSbTe-based thin films. A notable shift was observed in the orientation of the hkl planes from (015) to (1010) after heat treatment. This shift indicates a change in the preferred crystallographic orientation or texture of the films. The shift in the texture structure suggests that the heat treatment influenced the growth axis of the films. The change in preferred crystallographic orientation can be attributed to the rearrangement of atoms and the recrystallization processes that occurred during heat treatment. These processes can lead to the alignment of crystallographic planes along specific directions, resulting in a preferred orientation or texture. The influence of texture structure on the properties of thin films is significant. The orientation of crystallographic planes affects the anisotropic properties of the films, including electrical conductivity and thermal conductivity. In the case of thermoelectric materials, such as BiSbTe-based films, texture structure can influence the thermoelectric performance. Therefore, the observed shift in the hkl planes from (015) to (1010) indicates a change in the growth axis and suggests that the heat treatment influenced the texture structure of the BiSbTe-based thin films. This structural evolution has the potential to impact the thermoelectric properties of the films, and further investigations are warranted to explore the relationship between texture structure and thermoelectric performance.

AFM measurements were conducted on the BiSbTe-based thin film after vacuum annealing. The AFM measurements encompassed various parameters, including topography, amplitude, and frequency, which were analyzed to gain insights into the morphological changes induced by the annealing process. The topography analysis, as shown in Fig. 3a, provides a visual representation of the surface features and roughness of the thin films. It can be observed that the annealed films exhibit a smoother surface with reduced surface irregularities and roughness. This improvement in surface smoothness can be attributed to the recrystallization and restructuring processes that occur during the annealing process. The annealing treatment likely facilitates the removal of surface defects and the enhancement of atomic ordering, resulting in a more uniform and less rough surface topography. The amplitude and frequency analyses, also presented in Fig. 3b and c, provide information about the surface properties and the presence of surface variations on a nanoscale level. After vacuum annealing, it can be noted that the amplitude and frequency of surface variations are reduced compared to the as-deposited films. This reduction suggests a decrease in the occurrence of surface defects, such as grain boundaries, dislocations, or other forms of surface roughness [13, 14]. The annealing process likely promotes the healing and restructuring of the thin films, resulting in a more homogeneous and smoother surface at the nanoscale level.

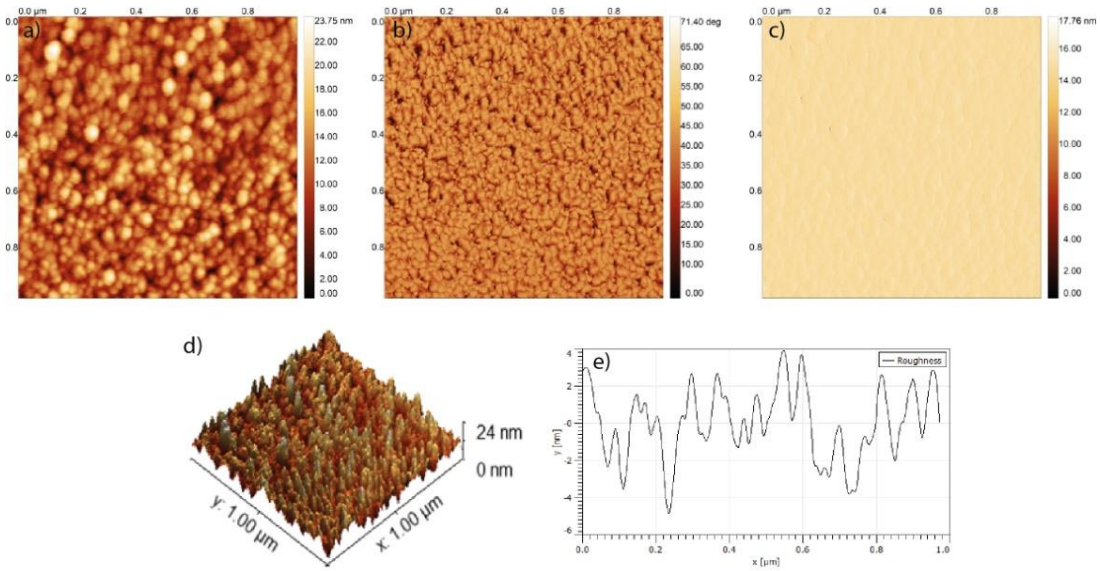


Fig 3. AFM measurements of high-vacuum annealed at 250°C thin films a) topography, b) amplitude, c) frequency, d) 3D perspective and e) the roughness measurement for 1µm line

The 3D-AFM and roughness measurements reveal that the vacuum annealing treatment has a beneficial effect on the morphological properties of the BiSbTe-based thin films as seen Fig. 3d and e. The annealed films exhibit improved surface smoothness, reduced surface irregularities, and decreased surface variations at both micro and nanoscale levels. These morphological changes are indicative of the restructuring and recrystallization processes occurring during annealing, which contribute to the improved surface quality and homogeneity of the films. The observed morphological improvements have significant implications for the thin films' overall performance, particularly in energy harvesting applications. A smoother and more uniform surface topography can enhance the contact between the thin film and other components in a device, leading to improved electrical and thermal transport properties and ultimately enhancing the efficiency of energy conversion. AFM measurements of the BiSbTe-based thin film after vacuum annealing provide valuable insights into the morphological changes induced by the annealing process [14]. The annealed films exhibit smoother surface topography, reduced surface irregularities, and decreased surface variations at both micro and nanoscale levels. These morphological improvements are beneficial for achieving enhanced performance in energy harvesting applications. Further investigations and complementary characterization techniques can provide additional quantitative information about the surface morphology and its correlation with the thin films' electrical, thermal, and energy harvesting properties.

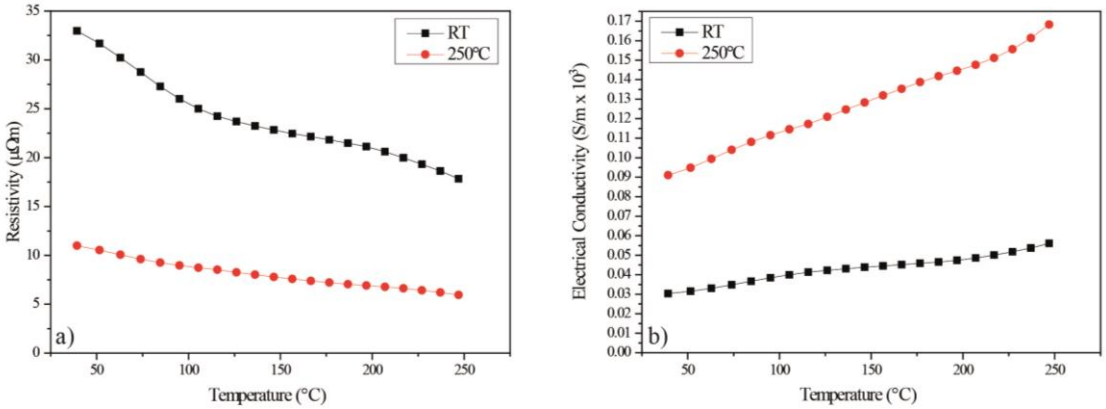


Fig 4. a) Resistivity and b) electrical conductivity for room temperature deposited and high-vacuum annealed at 250°C thin films

The temperature-dependent resistivity measurements were conducted to investigate the effect of heat treatment under vacuum on the electrical properties of the BiSbTe-based thin films. The measurements included both electrical resistance and electrical conductivity, which were analyzed before and after the heat treatment, as presented in Figs. 4a and 4b, respectively. The results of the resistivity measurements reveal significant changes in the electrical properties of the thin films after heat treatment. Comparing the electrical conductivity and electrical resistance values before and after heat treatment, it can be observed that the most notable change occurs at room temperature and also at high temperatures. After heat treatment, the electrical conductivity at room temperature increases approximately fourfold, while the electrical resistance also increases by a similar factor. This change indicates an overall reduction in the electrical conductivity of the films after heat treatment. At higher temperatures, the differences become even more pronounced. The electrical conductivity at elevated temperatures after heat treatment increases up to 4 times compared to the pre-heat treatment state, same as the electrical resistance shows. This significant increase in both electrical conductivity and resistance at high temperatures suggests a substantial modification in the electrical transport properties of the thin films induced by the heat treatment process [6].

The observed changes in electrical conductivity and resistance can be attributed to several factors. Heat treatment under vacuum is known to induce structural changes in thin films, such as recrystallization, grain growth, and the removal of defects [15, 16]. These structural modifications can alter the electronic and phonon scattering mechanisms within the material, affecting the overall electrical transport behavior. The increase in electrical resistance and decrease in electrical conductivity after heat treatment indicate an increase in the scattering of charge carriers, impeding their mobility. This can be attributed to changes in the crystal structure, grain boundaries, and defects present in the films. The enhanced scattering phenomena lead to an overall reduction in electrical conductivity and an increase in electrical resistance. The temperature dependence of the electrical properties also highlights the role of heat treatment in altering the thermal activation energy of charge carriers. The substantial increase in electrical conductivity and resistance at high temperatures suggests a change in the energy barriers for charge carrier transport within the thin films. Further investigations and complementary analyses are warranted to gain a deeper understanding of the mechanisms underlying the observed changes in electrical properties and their correlation with the microstructural changes induced by heat treatment.

Conclusion

In conclusion, our research has provided valuable insights into the optimization of thermoelectric thin films for energy harvesting. Through extensive experimentation and analysis, it was observed that the utilization of BiSbTe thin films on rigid substrates resulted in an increased efficiency of a thermoelectric energy generator. This finding suggests that these thin films hold promise as effective energy harvesters. The investigation involved a comprehensive study of the physical and chemical properties of the BiSbTe thin films. Various characterization techniques were employed to assess their structural, electrical, and thermal properties. This included techniques such as X-ray diffraction (XRD), scanning electron microscopy (SEM-EDX), and electrical conductivity measurements. By thoroughly examining these properties, a deeper understanding of the material's behavior and its potential for energy harvesting applications was achieved. To enhance the performance of the BiSbTe thin films, a range of processing and fabrication techniques were developed and employed. These techniques aimed to optimize the film's structure, composition, and morphology, ultimately improving its thermoelectric properties. The effects of heat treatment and other processing parameters were investigated to identify the optimal conditions for achieving high-performance thin films. The application of these BiSbTe thin films in power generation was explored.

By identifying key parameters and conducting rigorous experiments, it is possible to fabricate thin films with superior performance compared to traditional energy sources. With continued refinement and optimization, thermoelectric thin films have the potential to become a reliable, efficient, and cost-effective solution for energy harvesting applications, contributing to a more sustainable and greener future. We have identified several key parameters that must be considered in order to optimize the performance of these materials and have conducted a range of experiments to illustrate their importance. As a result, we are able to produce thermoelectric thin films with superior performance compared to traditional energy sources. The results of this investigation indicated that it is possible to fabricate thermoelectric thin films with performance levels comparable to bulk thermoelectric materials, making them a viable alternative in energy harvesting applications. With

further optimization and refinement, thermoelectric thin films could become a reliable and cost-effective energy harvesting solution.

Acknowledgments

This work was supported by the Scientific and Technological Research Council of Turkey (TUBITAK) with project number 221M470.

References

1. H. Julian Goldsmith, Thermoelectric Refrigeration. Plenum, New York. 1964.
2. G.D. Yüzüak, C. Karagöz, E. Yüzüak, Exploring the sputtering conditions in ZnO thin film for triboelectric nanogenerator electrode. International Journal of Energy Research 46 (14) 20494-20500.
3. M.G. Kanatzidis Nanostructured thermoelectrics: The new paradigm, Chem. Mater., 22 (2010) 648-659.
4. M.A. Zoui, S. Bentouba, J.G. Stocholm, M. Bourouis A review on thermoelectric generators: progress and applications Energies. 13 (2020) 3606.
5. L. Yang, Z.G. Chen, M.S. Dargusch, J. Zo u High performance thermoelectric materials: progress and their applications. Adv. Energy Mater., 8 (2018) 1701797.
6. G.D. Yüzüak, M.M. Çiçek, Y.Elerman, E. Yüzüak, Enhancing the power factor of p-type BiSbTe films via deposited with/without Cr seed layer. Journal of Alloys and Compounds 886 15 (2021) 161263.
7. T. Mori, Novel principles and nanostructuring methods for enhanced thermoelectrics. Small, 13 (2017) 1702013.
8. A.L. Bassi, A. Bailini, C.S. Casari, F. Donati, A. Mantegazza, M. Passoni, V. Russo, C.E. Bottani, Thermoelectric properties of Bi–Te films with controlled structure and morphology. J. Appl. Phys., 105 (2009) 124307.
9. L. Mulder, H. van de Glind, A. Brinkman, O. Concepción, Enhancement of the Surface Morphology of (Bi0.4Sb0.6)2Te3 Thin Films by In Situ Thermal Annealing. Nanomaterials 2023, 13, 763. https://doi.org/10.3390/nano13040763
10. P. Bhatnagar, D. Vashaee, Development of MEMS Process Compatible (Bi,Sb)2(Se,Te)3-Based Thin Films for Scalable Fabrication of Planar Micro-Thermoelectric Generators. Micromachines 2022, 13, 1459. https://doi.org/10.3390/mi13091459
11. W-Y. Lee, M-S. Kang, N-W. Park, G-S. Kim, H-W.Jang, E. Saitoh, and S-K. Lee, Phase and Composition Tunable Out-of-Plane Seebeck Coefficients for MoS2-Based Films. ACS Applied Electronic Materials 2022 4 (4), 1576-1582. https://doi.org/10.1021/acsaelm.1c01260
12. S. Elyamny, N.G. Imam, G. Aquilanti, H. Cabrera, A.El-H. B. Kashyout, Thermal transport properties for unveiling the mechanism of BiSbTe alloys in thermoelectric generation: A glance from synchrotron radiation Bi L3-XAFS. Journal of Materials Research and Technology, 18 (2022) 2261-2272. https://doi.org/10.1016/j.jmrt.2022.03.101
13. A. Behera, S. Aich, Characterisation and properties of magnetron sputtered nanoscale bi-layered Ni/Ti thin films and effect of annealing. Surf. Interface Anal. 47 (2015) 805–814. https://doi.org/10.1002/sia.5777
14. B. Attila and P. Lehoczki, An AFM study regarding the effect of annealing on the microstructure of gold thin films. Proceedings of the 36th International Spring Seminar on Electronics Technology (2013) 317-322.
15. M. Surmeneva, K. Prosolov, I. Glukhov, I. Grubova, V. Botvin, R. Surmenev, Y. Sharkeev, Effects of annealing in vacuum on the microstructure of silicon-containing calcium phosphate films deposited on a ZrNb alloy by radio-frequency magnetron sputtering, Vacuum, 212 (2023) 112028. https://doi.org/10.1016/j.vacuum.2023.112028
16. C. Sudarshan, S. Jayakumar, K. Vaideki, C. Sudakar, Thin Solid Films, 629 (2017) 28-38. https://doi.org/10.1016/j.tsf.2017.03.043

LIST OF PARTICPANTS

	Name	University	Country
1.	Nora de Leeuw	University of Leeds	UK
2.	Mosbah Zidani	University of Batna2	Algeria
3.	Sergey V. Dorozhkin	Kudrinskaja sq. 1-155	Russia
4.	Dragan P. Uskoković	Institute of Tech. Sciences of SASA	Serbia
5.	Ozkan Gokcekaya	Osaka University	Japan
6.	Filiz Ercan	Abdulrahman Bin Faisal University	Saudi Arabia
7.	Azeez Abdullah Barzinjy	Soran University	Iraq
8.	Burhan Ateş	Inönü University	Türkiye
9.	İsmail Ercan	Düzce University	Türkiye
10.	Savaş Kaya	Cumhuriyet University	Türkiye
11.	Süleyman Köytepe	Inönü University	Türkiye
12.	Ahlem Abidi	University of Tunis El Manar	Tunisia
13.	Ben Ammar Ben Khadda	University of Biskra	Algeria
14.	Naveed Zafar Ali	Quaid-I-Azam University	Pakistan
15.	A. Khelifa Baghdouche	Université 20 août 1955	Algeria
16.	Sammia Shahid	University of Management and Tech.	Pakistan
17.	Mounir Sakmeche	University of Adrar	Algeria
18.	Rebaz Obaid Kareem	Halabja University	Iraq
19.	Zaiem Slimane	University of Batna1	Algeria
20.	Mokhtar Nebab	University M'H. B. of Boumerdès	Algeria
21.	Niyazi Bulut	Firat University	Türkiye
22.	Mediha Kök	Firat University	Türkiye
23.	Hülya Güneş Ateş	Firat University	Türkiye
24.	O. Abdulrahman Hamad	University of Raparin	Iraq
25.	Mert Altundal	Boğaziçi University	Türkiye
26.	Ali Çiriş	Niğde Ömer Halisdemir University	Türkiye
27.	Ecem Özen	Fırat University	Türkiye
28.	Meltem Coşkun	Fırat University	Türkiye
29.	Alev Taze	Fırat University	Türkiye
30.	Kathrin S. Mohammed	University of Raparin	Iraq
31.	Dine Sarıateş	Fırat University	Türkiye

32.	M. Sait Kanca	Munzur University	Türkiye
33.	Merve Özcan	Toros University	Türkiye
34.	Melikehatun Fırat	Fırat University	Türkiye
35.	Mehmet Çelik	Fırat University	Türkiye
36.	Ahmet Doğan	Fırat University	Türkiye
37.	Serhat Keser	Fırat University	Türkiye
38.	Tuğrul Yumak	Sinop University	Türkiye
39.	Yasemin Merve Ayhan	Malatya Turgut Ozal University	Türkiye
40.	Binnur Şahin	Malatya Turgut Ozal University	Türkiye
41.	Yusuf Şamil Tekin	Malatya Turgut Ozal University	Türkiye
42.	Emine Nur Acar	Malatya Turgut Ozal University	Türkiye
43.	Tuğçe Akyüz	Malatya Turgut Ozal University	Türkiye
44.	Burhan Tarık Çetin	Malatya Turgut Ozal University	Türkiye
45.	Tankut Ateş	Malatya Turgut Ozal University	Türkiye
46.	Turan İnce	Fırat University	Türkiye
47.	Fatih İsen	Fırat University	Türkiye
48.	Emrullah Kamışlıoğlu	Fırat University	Türkiye
49.	Mehmet Mürşit Temüz	Fırat University	Türkiye
50.	Serpil Yalçın Kuzu	Fırat University	Türkiye
51.	Ceylan Alkaya	Cumhuriyet University	Türkiye
52.	Serdar Acar	Fırat University	Türkiye
53.	Muzaffer Güngören	Fırat University	Türkiye
54.	Adnan Aldemir	Van Yüzüncü Yıl University	Türkiye
55.	Gizem Durak Yüzüak	Recep Tayyip Erdoğan University	Türkiye
56.	Hazal Aktaş	AkzoNobel Kemipol	Türkiye
57.	Tuğba Güngör Ertuğral	Çanakkale Onsekiz Mart University	Türkiye
58.	Vahit Gür	Fırat University	Türkiye
59.	Cemre Kocahakimoğlu	AkzoNobel Kemipol	Türkiye
60.	Sevim Bilici	Bandirma Onyedi Eylul University	Türkiye
61.	Riyadh Saeed Agid	Salahaddin University	Iraq
62.	Nassima Chekroun	Abou Bekr Belkaid University	Algeria
63.	Murat Bozkurt	Fırat University	Türkiye
64.	Mikail Dönmez	Fırat University	Türkiye
65.	Mustafa Kaya	Fırat University	Türkiye
66.	Sultan Erkan	Cumhuriyet University	Türkiye
67.	Ismail Cem Kantarlı	Ege University	Türkiye
68.	Ercan Ercan	Bitlis Eren University	Türkiye

69.	Uğur Köroğlu	Hacettepe University	Türkiye
70.	Alper Biçer	Tokat Gaziosmanpaşa University	Türkiye
71.	Kenan Koran	Fırat University	Türkiye
72.	Cihat Aydın	Fırat University	Türkiye
73.	Boubekeur Razika	Université de Tlemcen	Algeria
74.	Dinara Khairutdinova	Russian Academy of Sciences	Russia
75.	Margarita Goldberg	Russian Academy of Sciences	Russia
76.	Nadezhda Donskaya	Russian Academy of Sciences	Russia
77.	Alexander Fomin	Russian Academy of Sciences	Russia
78.	O.S. Antonova	Russian Academy of Sciences	Russia
79.	Anatoliy A. Konovalov	Russian Academy of Sciences	Russia
80.	E.A. Eseva	Russian Academy of Sciences	Russia
81.	P.D. Polikarpova	Russian Academy of Sciences	Russia
82.	A.V. Akopyan	Russian Academy of Sciences	Russia
83.	Vladimir S. Komlev	Russian Academy of Sciences	Russia
84.	E.D. Nosova	Russian Academy of Sciences	Russia
85.	P.A. Krokhicheva	Russian Academy of Sciences	Russia
86.	Işık İpek Avcı Yayla	Istanbul Technical University	Türkiye
87.	Amel Kouache	CRTI	Algeria
88.	Özge Öztarakçı	Cumhuriyet University	Türkiye
89.	Ebru Yüce Babacan	Munzur University	Türkiye
90.	İlknur Baldan Işık	Çukurova University	Türkiye
91.	Tabti Affaf	Relizane University	Algeria
92.	Auwalu Sa'ıdu	Fırat University	Türkiye
93.	Demet Coşkun	Fırat University	Türkiye
94.	Abderrazzak Baba A.	Relizane University	Algeria
95.	Erkan Karataş	Erzurum Technical University	Türkiye
96.	Gonca Ateş	Şırnak University	Türkiye
97.	Erhan Karaca	Hacettepe University	Türkiye
98.	Handan Aydın	Munzur University	Türkiye
99.	Ala Hamd Hssain	Halabja University	Iraq
100.	Beyhan Kemaloglu	Fırat University	Türkiye
101.	Narimene Mansouri	University Chadli Bendjedid El Tarf	Algeria
102.	Wissem Haffaf	University Abubekr Belkaid	Algeria
103.	Seçil Sevim Ünlütürk	Kansai Altan Boya Sanayi	Türkiye
104.	İlayda Melek Çelik	Kansai Altan Boya Sanayi	Türkiye
105.	Necati Güdümcüoğlu	Kansai Altan Boya Sanayi	Türkiye

106.	Fatih Ahmet Çelik	Bitlis Eren University	Türkiye
107.	Ayça Kıyak Yıldırım	Bilecik Şeyh Edebali University	Türkiye
108.	Ibrahim Isah Nasidi	Fırat University	Türkiye
109.	Alev Taze	Fırat University	Türkiye
110.	M. Savaş Ellidokuzoglu	Yıldız Technical University	Türkiye
111.	Pınar Demir	Fırat University	Türkiye

Last updated (CET): 12 June 2023 04:39 PM